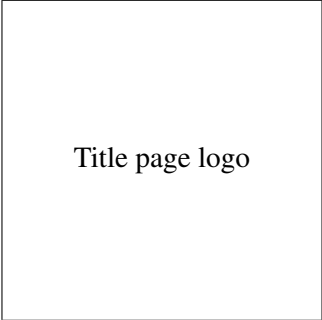


In situ X-Ray Spectroscopy of
Ethylene Epoxidation over Ag and
studies of Li-ion batteries and Cu
sulfidation

This Page will be Replaced before Printing



Title page logo

Dissertation presented at Uppsala University to be publicly examined in room 2005, Ångström laboratory, Lägerhyddsvägen 1, Polacksbacken, Uppsala, Sweden, Tuesday, November 5, 2013 at 09:15 for the degree of Doctor of Philosophy. The examination will be conducted in English.

Abstract

This thesis is based on experiments applying synchrotron based X-ray Absorption Spectroscopy (XAS) and Resonant Inelastic X-ray Scattering (RIXS) in the soft X-ray region to energy related systems.

The main work of this thesis has been to develop a reaction cell that allowed for *in situ* XAS and RIXS investigations of the partial epoxidation of ethylene over a Ag catalyst at 1 atm and up to 250°C. The developed *in situ* cell can be used in two sample modes: 1) the Ag catalyst is deposited directly onto the vacuum separating membrane with the reaction gases flowing beneath it or 2) a slightly compressed Ag powder sample is at a distance to the vacuum membrane with the reaction gases flowing between the Ag powder sample and the membrane. Both sample modes offers the total fluorescence yield, TFY, and the total electron yield, TEY, to be recorded simultaneously.

By means of the developed *in situ* cell a number of oxygen species, residing in/on the Ag surface or in the Ag bulk, have been detected. We claim to detect adsorbed O₂ under epoxidation conditions, as well as Ag–O–H groups. We are also able to monitor changes of the absorbed oxygen as we change the composition of the reaction gas feed.

The first charging cycle of Li-ion batteries have been investigate by *ex situ* measurements on the cathode Li_{2-x}MnSiO₄ and the anode composite Li_xNi_{0.5}TiOPO₄/C. The initial crystalline material becomes amorphous due to lithiation during the first first charging. We find that the redox behaviors of these two states are significantly different.

Sulfidation of natural copper oxides are is found to be strongly promoted when it is grown on the host metal by a disproportionation.

Paw Toldbod Kristiansen, Department of Physics and Astronomy, Uppsala University, Box 530, 75121 Uppsala, Sweden

© Paw Toldbod Kristiansen 2013

List of papers

This thesis is based on the following papers, which are referred to in the text by their Roman numerals.

- I **Reaction cell for *in situ* soft x-ray XAS and RIXS measurements of heterogeneous catalysis up to 1 atm and 250°C**
P. T. Kristiansen, T. C. R. Rocha, A. Knop-Gericke, J.H. Guo, and L. C. Duda
Submitted to Rev. Sci. Instrum.
- II ***In situ* soft x-ray spectroscopy of ethylene epoxidation over Ag**
P. T. Kristiansen, T.C.R. Rocha, A. Knop-Gericke, R. Schlögl and L. C. Duda
In manuscript
- III **X-ray absorption spectroscopy and resonant inelastic scattering study of the first lithiation cycle of the Li-ion battery cathode $\text{Li}_{2-x}\text{MnSiO}_4$**
P. T. Kristiansen, M. Dahbi, T. Gustafsson, K. Edström, D. Newby, K.E. Smith and L. C. Duda
Submitted to PCCP
- IV **X-ray absorption spectroscopy and resonant inelastic scattering study of the first lithiation cycle of the Li-ion battery anode material $\text{Li}_x\text{Ni}_{0.5}\text{TiOPO}_4/\text{C}$**
P. T. Kristiansen, M. Dahbi, I. Saadoune, T. Gustafsson, K. Edström, K.E. Smith and L. C. Duda
In manuscript
- V **A Combined Experimental and *ab initio* Multi Reference Configuration Interaction study of the Resonant Inelastic X-Ray Scattering spectrum of CO_2**
D. Maganas, P. T. Kristiansen, L. C. Duda, A. Knop-Gericke, S. DeBeer, R. Schlögl and F. Neese
Submitted to PCCP
- VI **X-ray spectroscopy of selected Cu(II) compounds exposed to dilute sulfide solutions**
P. T. Kristiansen, F. Massel, L. Werme, C. Lilja and L. C. Duda
In manuscript

VII Exposure of Oxidized Copper Surfaces to Aqueous Na₂S Solution Studied with Soft X-Ray Spectroscopy

H. M. Hollmark, J. R. Vegelius, P. T. Kristiansen, L. Werme, and L. C. Duda

J. Electrochem. Soc. 2011 volume 158, issue 1, C1-C5

VIII Sub-band gap electronic states in nanocrystalline WO₃ thin films studied by soft x-ray spectroscopy, optical absorption spectroscopy and density functional calculations

M. B. Johansson, P. T. Kristiansen, G. Baldissera, L. Duda, C. Persson, G.A. Niklasson and L. Österlund

In manuscript

Reprints were made with permission from the publishers.

Contents

1	Comments on my participation	9
2	Introduction	11
3	Experimental Considerations	12
3.1	Applied soft x-ray spectroscopy techniques	12
3.2	Instrumental developments	17
4	Heterogeneous catalysis	25
5	Results	30
5.1	Ethylene epoxidation over Ag	30
5.2	RIXS studies of CO ₂ and C ₂ H ₄ O	44
5.3	Photocatalytic transition metal oxide films	47
5.4	Water splitting with precious metal oxides	54
5.5	Li-ion batteries	56
5.5.1	Introduction	56
5.5.2	The anode material Li _x Ni _{0.5} TiOPO ₄ /C	56
5.5.3	The cathode material Li _{2-x} MnSiO ₄	58
5.6	Sulfidation of natural Cu oxides	59
6	Conclusions and Outlook	60
7	Summary in Swedish	61
	References	62

1. Comments on my participation

My contributions to the included manuscripts/articles are given here

Paper I on the developed *in situ* cell for heterogeneous catalysis: I did the multiple designs leading to the final cell (the CAD was done by C. J. Englund, engineer), the epoxidation beamtime proposals (except for the first to BESSY and the first to ALS), did the principal synchrotron work (together with Dr. Rocha or the main-supervisor), the data treatment and wrote up the manuscript (in close collaboration with the main-supervisor).

Paper II on *in situ* x-ray spectroscopy of ethylene epoxidation over Ag: I did the beamtime proposals (except for the first to BESSY and the first to ALS), did the principal synchrotron work (together with Dr. Rocha or the main-supervisor), the data treatment and wrote up the manuscript (in close collaboration with the main-supervisor).

Paper III on the Li-ion cathode $\text{Li}_{2-x}\text{MnSiO}_4$: I did the synchrotron work, the synchrotron data treatment and wrote up the manuscript (in close collaboration with the main-supervisor).

Paper IV on the Li-ion anode $\text{Li}_x\text{Ni}_{0.5}\text{TiOPO}_4/\text{C}$: I did the synchrotron work, the synchrotron data treatment and wrote up the manuscript (in close collaboration with the main-supervisor).

Paper V on symmetry breaking of CO_2 : I did the beamtime proposal (originally the measurements were intended as support measurements for the epoxidation project), did the principal synchrotron work (together with the main-supervisor), I prepared the experimental data and did little editing in the manuscript.

Paper VI on Cu sulfidation: I did the synchrotron work, the synchrotron data treatment and took part in writing the manuscript (together with L. Werme and the main-supervisor).

Paper VII on Cu sulfidation: I participated in the beamtime and I did the SEM.

Paper VIII on band gap states in WO_3 : I co-authored the beamtime proposals, did the principal synchrotron work, prepared the synchrotron data and did some editing/additions in/to the manuscript.

The PhD project has in a whole been conducted as a collaboration between The Fritz Haber Institute of the Max Planck Society (FHI) at the department of Inorganic Chemistry, in the group of Electronic Structure, under Dr. Axel

Knop-Gericke whom also has been a co-supervisor, and Uppsala University at the department of Physics and Astronomy in the group of Molecular and Condensed Matter Physics with docent Laurent Duda as main-supervisor and professor Jan-Erik Rubensson as co-supervisor.

The general supervision and cooperation of Laurent, the main-supervisor, in all of my doings are greatly acknowledged.

2. Introduction

The main intent of this thesis is to spectroscopically study chemical reactions in real time. In the past such studies were often conducted by e.g. performing a reaction on surface, in an environment that suited that particular reaction, and then transfer the surface to an ultra high vacuum environment in which spectroscopy is normally performed. This approach has obvious shortcomings which could be overcome if the environment of the investigated reaction was made compatible with the environment of the spectroscopy - exactly this has been the main challenge of this thesis.

The chemical reactions that are in the focus of this thesis are heterogeneous catalysis where gas species, or liquid, meet on solid surface that catalytic facilitate a reaction between the gas species. The energy input for such reactions can be e.g. heat or UV-irradiation.

Most effort has gone into investigating the partial oxidation of ethylene to ethylene oxide, EO, over an Ag catalyst. This reaction is in particular well suited for *in situ* investigations as transient species are expected to play a central role in the epoxidation process.

For the *in situ* measurements we employ X-ray absorption spectroscopy (XAS) and resonant inelastic X-ray scattering (RIXS) because of their selective properties: XAS is both an element and a chemically specific technique and in addition to this RIXS also offers site selectivity. Soft X-rays offer the advantage of having a larger probing depth than electrons allowing the use of thin X-ray transparent membranes. Compared to hard x-rays this still poses a challenge because the probed catalytic material must be very close to the membrane.

Apart from the main project of ethylene epoxidation X-ray spectroscopy is also applied to other systems, namely Li-ion battery cycling and Cu oxide sulfidation. When employing XAS and RIXS to the battery cathode or anode one can obtain detailed information on where the electrons are positioned as the battery is charged or discharged.

3. Experimental Considerations

3.1 Applied soft x-ray spectroscopy techniques

In this chapter the experimental techniques applied for my PhD are presented in a phenomenological manner. In-depth descriptions of XAS is given in [1], of XES in [2] and of RIXS in [3].

The three techniques are employed in the soft x-ray regime, i.e. sub-keV photon energies. The life time broadening for the involved core hole excitations is relatively small (a few tenths of an electron volt) and their fluorescence yields are relatively high for transitions with chemical information. High energy x-ray fluorescence often has a higher yield but contains little chemical information and shorter core hole life times.

XAS

XAS usually requires a synchrotron radiation facility, where it is a relatively simple measurement to perform, by using a tunable monochromatic photon source and a means for detection of decay products. Fig. 3.1 shows the x-ray absorption process in the atomic case.

For solids, the absorption cross section depends crucially on the density of unoccupied states close to the Fermi level, i.e. the conduction band. Strong absorption occurs when the incident energy is sufficient to promote a core electron into the unoccupied orbitals, this is called an absorption edge. Dipole selection rules allow then to project the partial density of states, i.e. those of specific orbital symmetry. For instance, O K-XAS in oxides involves transitions between the O 1s core hole and states of p-character that belong to hybridized oxygen-metal orbitals. Thus the number of core holes reflect the partial unoccupied density of states of the conduction band.

The core hole subsequently decays via two possible channels: i) Auger electron emission or ii) x-ray fluorescence.

i) The main core hole decay channel (typically 99.9 %) is Auger electron production. By inelastic scattering, the high energy Auger electron causes a cascade of lower energy secondary electrons, which eventually leave the sample and generate a drain current in a solid. The drain current, which is proportional

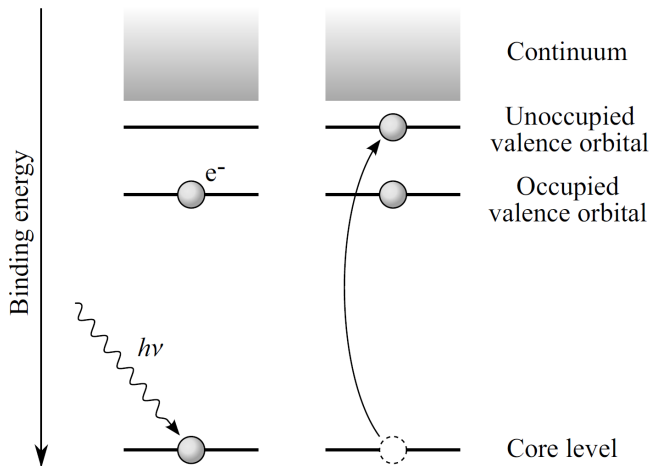


Figure 3.1. A schematic representation of the absorption step of XAS in the atomic case. Resonant absorption occurs when the incident energy matches the energy difference of an occupied and unoccupied orbital under the condition of dipole symmetry selection rules, e.g. $\Delta l = \pm 1$. Figure adopted from [4].

to the number of core holes generated in the close vicinity of the sample surface (5 nm) [1], can be measured by an amperemeter, typically in the nA-range. This detection mode is called total electron yield (TEY).

ii) A small fraction of the core holes decay via x-ray fluorescence. This can be detected by a (commercially available) photodiode [5] and an amperemeter, typically in the high nA-range. This detection mode is called total fluorescence yield (TFY). The fluorescence x-rays have an attenuation length that is comparable to the incident x-rays. This entails that the information depth of the TFY mode (~ 100 nm in solids) is much larger than for the TEY mode. On the other hand, this leads to saturation effects that distort the spectral appearance, although diluted species will be less affected.

Figure 3.2 compares the atomic number dependence of Auger and fluorescence yield for the K- and L_3 -shells. The Auger (fluorescence) yield monotonically decreases (increases) with Z . Note that the core hole lifetime decreases with Z , which limits the regions of interest to narrow bands (shaded areas), namely the soft x-ray region.

Thus a XAS measurement on a solid yields information on the partial unoccupied density of states. The presence of a core hole may distort the ground state distribution (when screening is low), which might lead to rigid (upwards) shifts of spectral features ($Z+1$ approximation). On the other hand, it has been shown that the total area under a XAS spectrum nevertheless reflects the ground state occupancy of the empty bands.

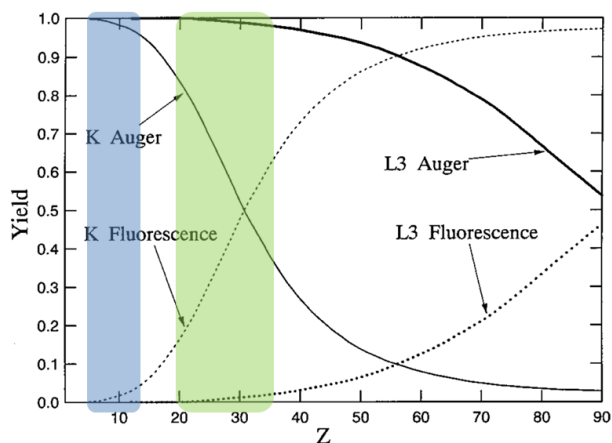


Figure 3.2. X-ray and Auger yields as a function of the atomic number, Z . The relevant K-edges are marked with blue and the relevant L-edges in green.

Experimentally, one scans the incident photon energy over an x-ray absorption edge, e.g. for the oxygen K edge. A suitable scan would be from 510 to 570 eV with the actual threshold being around 530 eV. The O K edge is particularly suited for XAS as the unoccupied states have a narrow energy distribution, due to the relative long lifetime of the core hole, which yields well defined features in the obtained intensity spectra. In contrast, the Ag $N_{2,3}$ core hole has a very short lifetime (leading to an energy broadening of over 10 eV), which obscures the chemical information in the XAS spectra.

XES and RIXS

The fluorescence decay of a core hole produces x-rays with a wavelength distribution that can be analyzed by a wavelength dispersive x-ray spectrometer [6]. This is called x-ray emission spectroscopy (XES). In XES information on the occupied density of states are retrieved. Figure 3.3 shows the XES process.

In the case the core hole excitation leads to ionization of the atom, the resulting spectra will be broadened by the core hole lifetime. For resonant excitation, the excited electron is promoted into a bound state and the incident x-ray energy is conserved locally. The latter is a prerequisite for resonant inelastic x-ray scattering (RIXS) to be strong. RIXS is a coherent second order photon scattering process [7] that does not suffer from core hole lifetime broadening. Thus, in principle, XES measurements do not require a tunable excitation source, e.g. an electron gun supplying electrons of sufficiently high energy to ionize the atom at the investigated edge.

Figure 3.4 shows the RIXS process. RIXS of 3d-transition metals (TM) display e.g. resonantly enhanced crystal field excitations at the TM L-edge. O

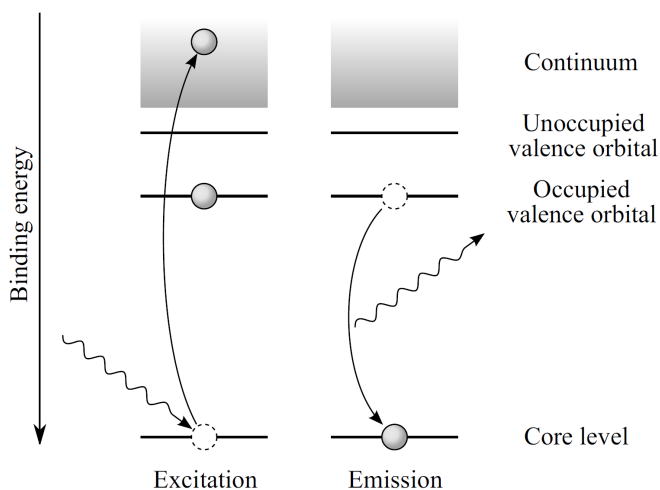


Figure 3.3. Schematic representation of XES in an atom: The atom is ionized by an x-ray photon (left panel). The created core hole is filled by a valence electron under the condition of dipole symmetry selection rules and a photon is emitted (right panel). The energy of the emitted photon reflects the energy difference of the orbitals. Figure adopted from [4].

K-RIXS for oxides can be used to project site specific occupied density of states (core hole free), which is particularly powerful in using RIXS as a fingerprint method for different oxygen species. As such RIXS, with its resonant character, is ideal suited for the *in situ* experiments described later where we attempt to get information from oxygen incorporated in Ag while gaseous O₂ is also present.

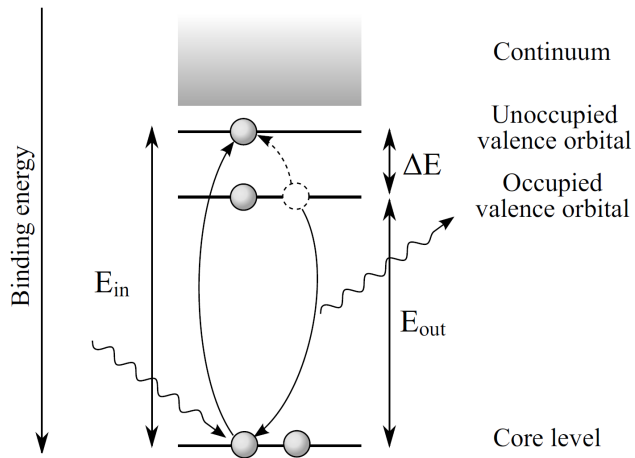


Figure 3.4. Schematic representation of RIXS in an atom: An x-ray photon is absorbed by an atom, promoting a core electron to an empty bound state orbital in the conduction band. An electron, often from an occupied orbital of the same symmetry, refills the core hole. Simultaneously, a photon is emitted. The atom is left a low-energy (typically less than a few eV) excited state. The energy of the atom corresponds to the energy difference between the photons. Figure adopted from [4].

3.2 Instrumental developments

In situ reaction cell

The developed cell is described in paper I. The *in situ* ethylene epoxidation data presented in this thesis were all obtained by the developed cell as sketched in figure 3.5 and 3.6 with either a thin film Ag sample, evaporated directly onto the membrane, or a Ag powder sample, figure 3.7 A) and B) respectively.

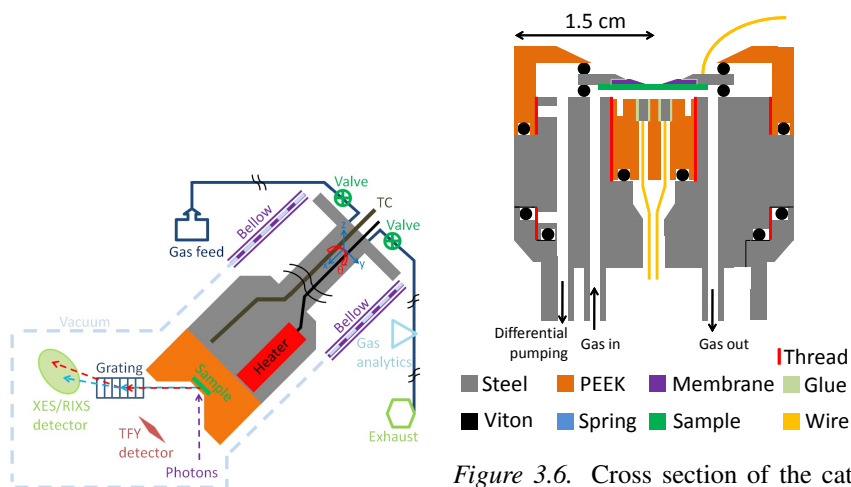


Figure 3.5. Schematic principle diagram of the cell system (not to scale).

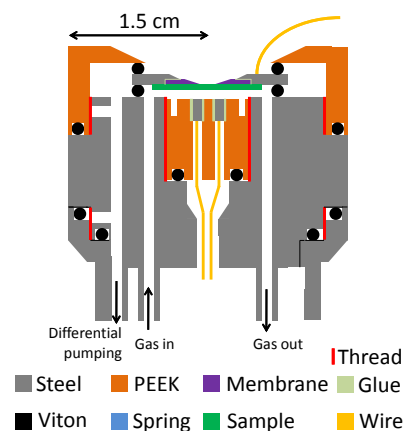


Figure 3.6. Cross section of the catalytic *in situ* cell. Here, the cell is shown in its configuration (A), where the catalytic material (green) is evaporated directly onto the membrane, which also serves as a gas–vacuum barrier. TEY is recorded by the wire connected to the membrane holding disk.

The inner PEEK part in figure 3.6 is exchangeable and is here shown with electric pads described below.

Figure 3.7 shows the photon probing vicinity A) with Ag film setup and B) with a Ag powder setup. In A) the photons passing through the film sample will travel their full attenuation length in the gas, so in this setup the gaseous O₂ contribution will be largely independent of the O₂ partial pressure. In B) the incoming photons pass a thin layer of gas before reaching the powder sample. Since the photons in B) travel a shorter distance than their attenuation length, it is necessary to keep the partial pressure of O₂ equal for all mixtures (we strived to adhere to this condition).

Figure 3.8 shows a scanning electron micrograph (SEM) of a post mortem Ag film sample. The Ag coated membranes used for *in situ* measurements prove

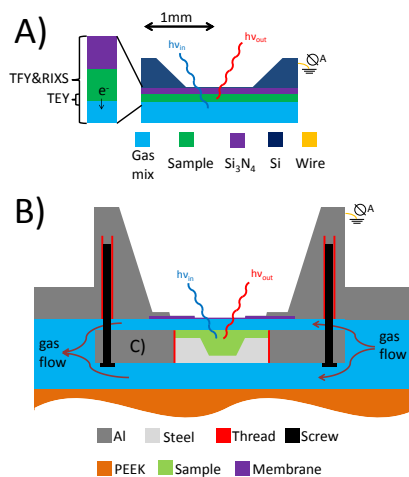


Figure 3.7. Schematic diagram (approximately to scale) of the cell parts close to the sample in configuration in the film-, A), and powder- configuration, B). The different probing depths/methods are indicated.

to be very fragile during cool down. Although great care was taken, all such membranes either break in the negative temperature ramp or when the pressure is equalized. Thus the black area is due to the missing membrane but a small fraction is retained in the lower right hand corner.

Locally, the probed membrane area is strongly heated, which has several causes: i) under reaction conditions, heterogeneous catalysis of ethylene is strongly exothermic, ii) the membrane has poor heat conductivity, and iii) the beam induces heating. This means that the temperature around the active Ag film is higher than the measured cell bulk temperature. The temperature increase is larger for a film sample than for a powder because the former is located on a low-conductivity Si₃N₄ membrane, which is not supported by the Si frame. One effect of this excess heating is seen in Fig. 3.8: the flowing gas has transported with it some of the excess heat of the membrane area, producing the circular shaded structures.

In Fig. 3.9 another effect of excess heating is evident: Ag island formation. This formation starts when the sample is exposed to a reaction mixture for the first time. This is detected by upcoming XAS features of gaseous O₂ (Rydberg dips in TFY around 540.5 eV). In order to get the largest possible signal from the Ag-absorbed oxygen species we moved the cell around to find a spot with the lowest 540.5 eV TFY dips.

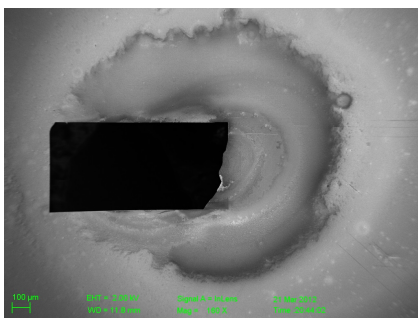


Figure 3.8. Scanning electron micrograph (SEM) of a uniformly 31 nm thick Ag film that has been applied for ethylene epoxidation at $T=225^{\circ}\text{C}$ with a total heat time of five days. The gas flow went from left to right.

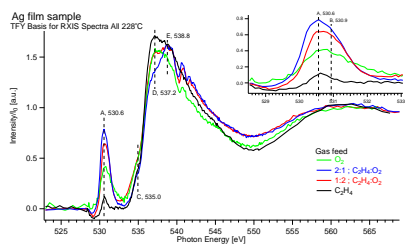


Figure 3.9. Scanning electron micrograph (SEM) from a fragment of membrane still attached to the Si frame after retrieval. Islandization is visible of a originally 25 nm thick Ag film that has been exposed to reaction conditions.

Security pinhole & Slit upstream of sample

This section describes a crucial improvement of the basic Nordgren spectrometer setup. For x-ray spectroscopy experiments at beamline U41-PGM at BESSY II we ship our own Nordgren type Rowland x-ray spectrometer endstation to Berlin, Germany. Initially, we used to separate the beamline vacuum physically from the endstation vacuum by a 100 nm thick Si_3N_4 membrane to protect the beamline vacuum, whenever measurements were performed on liquids and gases. This membrane absorbs $\sim 40\%$ of the photon intensity at the O K-edge. In order to avoid such a loss, a setup with a $\text{\O}100 \mu\text{m}$ pinhole was implemented, see Fig. 3.10 and Fig. 3.11.

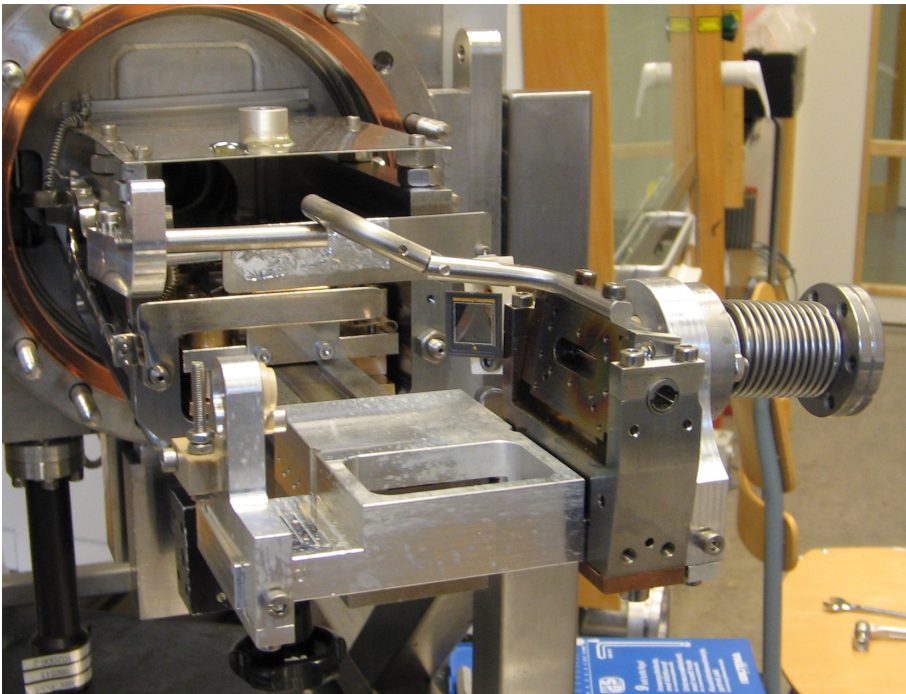


Figure 3.10. Photograph of the front part of the x-ray spectrometer. X-rays enter from right to left through the short bellows. The pinhole (not visible in the picture) is located in the bellows. Downstream of the pinhole is a variable-width horizontal slit that allows to baffle the beam in order to reduce the focal spot size.

Figure 3.11a shows the original setup of the spectrometer and Fig. 3.11b shows the modifications that were implemented. The security pinhole setup is based on two bellows. The first bellows is external and connects the beamline to the endstation vacuum chamber, which allows an alignment of the endstation. The other one is an internal bellows inside the endstation vacuum chamber, containing the pinhole, and clamped onto the optical axis. Using the spectrometer

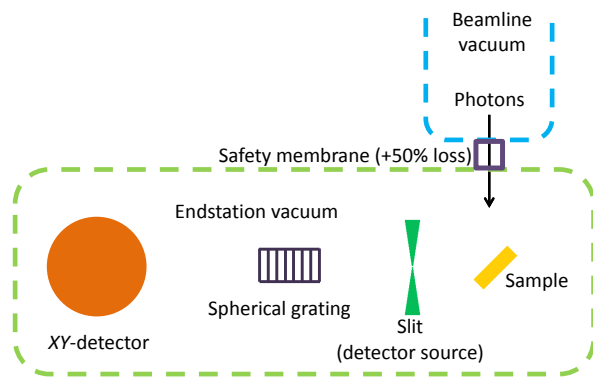
optical axis manipulator these bellows allows a fine adjustment of the pin hole position in order to let the beam pass the pinhole.

The pinhole disk is suspended in electrical isolation. Precise alignment of the pin hole can be achieved by monitoring and minimizing its drain current. All surfaces normal to the beam at the end of the internal bellows are covered with a fluorescent powder and there are fitted polished Si-wafer pieces at a 45° angle to the beam which enables a rough alignment by the eye.

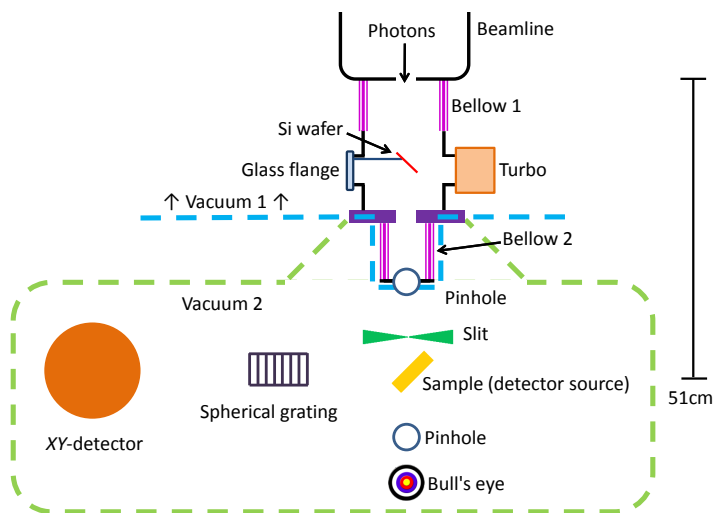
The performance of the security pinhole was tested by ramping the pressure on the endstation up and it was found that a beamline vacuum pressure did not exceed the high 10^{-8} mbar (with the last beamline valve closed) when the endstation vacuum was in the 10^{-3} mbar region.

Moving the slit upstream of the sample position means that the accepted solid angle of emission is maximized for a focal spot of a given diameter. Controlling the size of the spectrometer source in this manner also reduces the energy spread of the beam because the focal spot is energetically resolved vertically. With the monochromator exit slit at max, $3000 \mu\text{m}$, we found the vertical energy span of U41-PGM to be 8 eV at the Ni L-edge. In order to find this vertical energy span a Ni covered membrane was put in front of a fluorescent glass substrate, see Fig. 3.12(a), which in turn was placed in the path of the photons. A camera, external to the vacuum, was used to record the intensity of the beam as the photon energy was scanned across the Ni L-edge. Figure 3.12(b) shows the beam intensity at an energy where the Ni L-edge absorption happens at the beam center, marked with a green arrow. By monitoring when this absorption line began and ended it could be concluded that the vertical energy span is 8 eV.

A second aiming pinhole downstream of the sample position served to enable correct alignment of the spectrometer source on the Rowland circle (Fig. 3.11b) and allow reproducible positioning between beamtimes. The disk of the second pinhole is also covered with fluorescent powder, for rough alignment, and the drain current can be recorded for fine tuning. When the beam passes through the second pinhole it hits a metal "bull's eye" whose drain current is also recorded.



(a)



(b)

Figure 3.11. The GRAZE setup. (a) original setup with a safety membrane for *in situ* measurements on liquids and gases. (b) new pin hole setup.

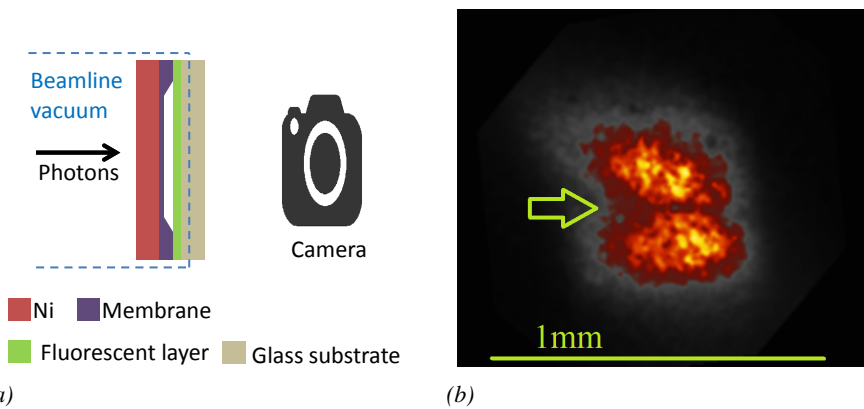


Figure 3.12. (a) setup for recording the energy resolution of the U41-PGMM beam. (b) snapshot at one energy with the absorbing area of the beam indicated.

Irradiation effects on the membrane

When measuring at the O K-edge behind a 100 nm thick Si_3N_4 membrane at an incident angle is 45° (giving a path length of 143 nm) only about 55% of the incoming photons are transmitted [8]. The energy uptake in the membrane is expected to lead to a significant temperature rise of the penetrated volume in the absence of heat conductivity.

$$H_{\text{Mem}} = \frac{535 \text{ eV} \cdot 10^{12} \text{ s}^{-1} \cdot 45\%}{710 \frac{\text{J}}{\text{kg K}} \cdot 100 \mu\text{m} \cdot 50 \mu\text{m} \cdot 100 \text{ nm} \cdot 3.2 \frac{\text{g}}{\text{cm}^3}} \approx 3.4 \cdot 10^6 \text{ K/s} \quad (3.1)$$

Si_3N_4 is a poor heat conductor (30 W/(m K)) compared to e.g. silver (429 W/(m K)). This entails that the temperature at the beam probing site is hard to determine experimentally. Figure 3.13 shows a SEM scan at an electron energy of 5 kV of an un-coated membrane used for gas phase measurements at room temperature. Clear signs of suspected beam heating seem to be observed. One should expect that such marks would not appear unless the local temperature had been close to the bulk decomposition temperature of Si_3N_4 (1900°C). Thus the penetrated volume has experienced a temperature considerable higher than the room temperature of the cell during the gas measurements. On the other hand, it is known ([9]) that the soft x-rays can cause the gaseous O_2 molecules to dissociate to atomic oxygen, which is an alternative explanation for the marks on the membrane.

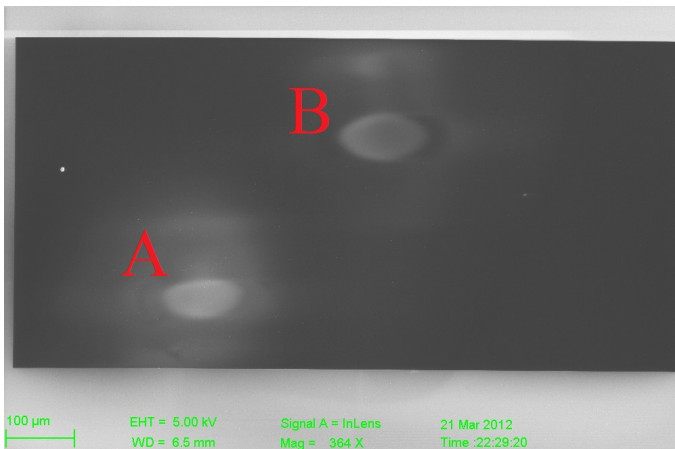


Figure 3.13. An un-coated 100 nm Si_3N_4 membrane used only for gaseous O_2 measurements at beamline 7 at the ALS. At the marked positions A and B it is clearly seen where the beam has penetrated the membrane.

This effect notwithstanding, we rarely experienced membrane failure during *in situ* experiments due to beam exposure.

4. Heterogeneous catalysis

Papers I, II and VIII concern heterogeneous catalysis, for which we present a short introduction here and is illustrated by the case of ethylene epoxidation over Ag.

A catalyst is a material that promotes a certain desired chemical reaction without undergoing a net reaction itself. Catalysts function by offering an alternative path to do a chemical reaction, that has a lower activation energy, E_a , than the non-catalytic path, see figure 4.1. As about 90% of all commercially produced chemical products involve catalysts at some stage in the process of their manufacture [10] gaining a higher understanding of catalysis is beneficial for society.

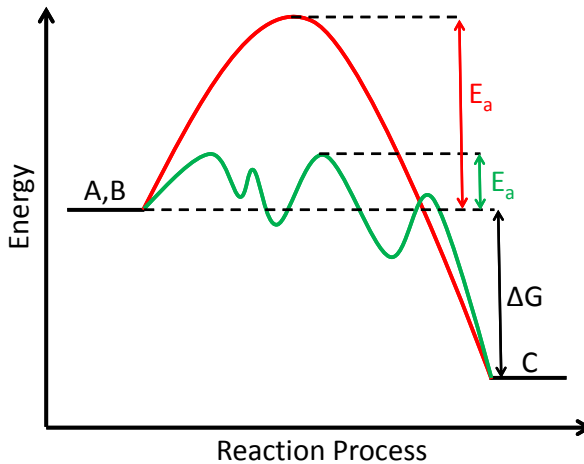


Figure 4.1. Energy profile of an un-catalytic (red trace) vs. a catalytic (green trace) path of an exothermic reaction. The free energy of A and B separately is larger than their product, C, however there is an energy barrier to overcome for the reaction to happen. Even though the catalytic path may consist of more steps, indicated by peaks, it has a lower E_a and will dominate the reaction.

We focus on heterogeneous catalysis, meaning that more than one phase is involved e.g. solids and gases, where the catalyst is a metal and the reactants are ethylene and oxygen or water. Generally the catalytic process can be divided into three stages:

- i The reactant molecules impinge on the surface of the metal catalyst and may bond to the metal if the anti-bonding states are pushed above the Fermi level [11] forming new bonding and anti-bonding states.
- ii The chemically adsorbed reactants, which are now bound to the surface of the catalyst, experience weaker internal bonds [12] and may now more easily bond to other surface species or molecules in the gas phase. In this stage the complexity of the reaction normally increases, as indicated by the many green peaks in figure 4.1, and often is only partially understood.
- iii Reaction products are formed and may desorb from the catalysts surface.

Ethylene epoxidation over Ag

EO is an immensely important chemical, it is produced by heterogeneous catalysis, of ethylene and oxygen over Ag, which is only partially understood. Improvement of our knowledge of this process is of both fundamental and commercial interest. EO is mostly used for synthesis of ethylene glycols, 65% of the total production [13], that in turn are used as antifreeze, in the production of polyester and polyethylene terephthalate (PET - raw material for plastic bottles). In 2008 the world wide production of EO was 19 Mt making it the 14th most produced organic chemical [14].

The industrial process utilizes a direct epoxidation of ethylene over an Ag catalyst, at 200 to 300°C and a total pressure of 10 – 30 atm, which on the face of it looks like a fairly simple reaction, see equation (4.1) and figure 4.2, where one oxygen atom is added to an ethylene molecule. However, the interplay between Ag, O₂ and C₂H₄ is somewhat complicated and still not fully understood. The challenge of understanding the industrial process is in particular great as the Ag is promoted with alkali or alkaline-earth elements combined with a trace feed of chlorine, which raises the selectivity of EO production, compared to combustion, to 80 – 85% where the pure Ag only yields 40 – 50%.

In order to gain insight on the electronic structure of the oxygen participating in the process spectroscopic techniques have been applied. Up until about the late 1990's the investigations was carried out on post reaction Ag samples and then *in situ* XPS measurements at few mbar became available. Thus there still existed a significantly pressure gap, a factor of > 2000, to the industrial process. The understanding gained by these measurements is the basis of the 2011 review, by Bukhtiyarov and Knop-Gericke [15], on the epoxidation process, which is briefly retold further below.

The main project of my PhD has been to develop and implement an epoxidation cell, described in section 3.2, that closes the pressure gap of the previous

in situ techniques. This is imperative to gain knowledge of the industrial process as the active species may be metastable and only exist, in detectable numbers, under atmospheric pressures [15]. Furthermore the *in situ* measurements of the cell should allow for measurements where information can be retained from the bulk of the active Ag by TFY/RIXS (and TEY) on the O K edge, as it has been suggested that subsurface/bulk oxygen species are crucial to the process [16]. The developed cell can accommodate both promoted and pure Ag samples, however we have solely measured on the latter. A natural next step would be measurements on e.g. Cu promoted Ag samples [17].

On an Ag catalyst the overall ethylene epoxidation follows the reaction outlined in (4.1), with the total oxidation of ethylene (4.2) and the secondary oxidation, (4.3), of EO acting as competing processes.

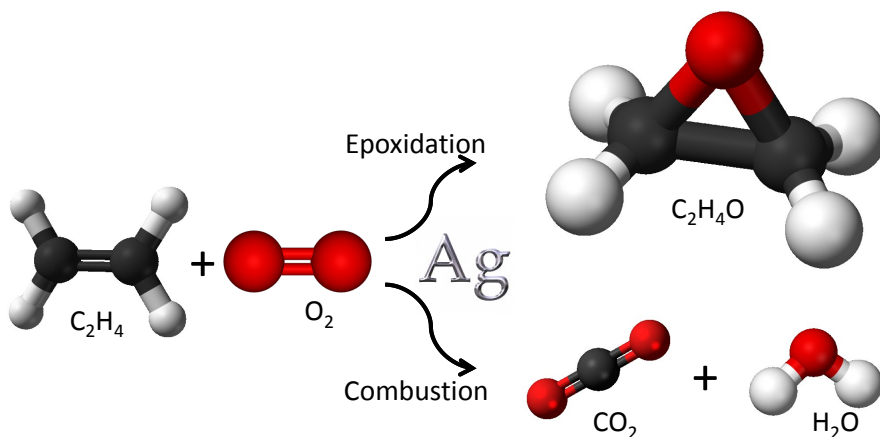
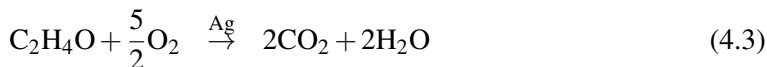
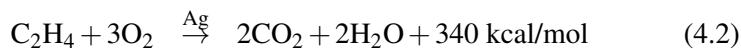
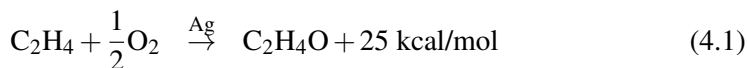


Figure 4.2. Stick and ball model of the overall primary reactions. The epoxidation is initiated by an activation of a C–C bond by O_{elec} and the combustion is initiated of a C–H activation by O_{nuc} .

By 1 mbar OK XPS measurements on the ongoing reaction at 147°C [18] two oxygen species could be detected which were labeled to surface adsorbed atomic nucleophilic oxygen, O_{nuc} , and to surface adsorbed atomic electrophilic oxygen, O_{elec} . O_{nuc} creates positive Ag sites ($\text{Ag}^+ - \text{O}^{2-} - \text{Ag}^+$) that are needed to bind ethylene to the Ag surface and can activate the C–H bond in ethylene,

which leads to combustion. O_{elec} can be described as an O^- anion that attacks the π -bond in ethylene leading to epoxidation. So the epoxidation requires both O_{nucl} to catch the ethylene and O_{elec} that will interact with the ethylene π -system to form EO that then desorbs. The O_{elec} supply to the ethylene adsorption site occurs by kink migration where the O_{elec} is localized,



An increase of the temperature to 197°C during reaction leads to two additional species detectable by *in situ* XPS assigned to O_γ and subsurface oxygen, O_{ss} . The γ assignment is based on thermal desorption spectroscopy as such gave three peaks labeled O_α originating from a surface species at 303°C (which covers both O_{nucl} and O_{elec}), a bulk-dissolved species, O_β , at 427°C and an interface species at 627°C, O_γ . The subsurface oxygen species, O_{ss} , is embedded in octahedral holes [19]), which is located in the surface/bulk interface and is non-reactive towards ethylene, an accumulation of this species causes a decrease of the EO formation rate. O_{ss} functions as a transport species, from where surface species are replenished and which is fed by bulk-dissolved oxygen, O_β . The amount of O_β increases with decreasing particle size, there is $\sim 1.6 \Theta$ (monolayer) of exchangeable oxygen in normal Ag powder (at grain sizes above ~ 50 nm Ag behaves as bulk for this reaction) and $\sim 6.0 \Theta$ in $\text{Ø}22$ nm Ag powder, why it may be presumed that the O_β species is localized in defect rich phases (that is a characteristic of small particles) or along grain boundaries.

Transformations between the different oxygen species have been suggested to follow a scheme as the one depicted in figure 4.3 [20, 21]. O_{nucl} is assumed to be formed directly by the dissociative adsorption of molecular oxygen. This is not the case for O_{elec} as the formation of EO happens with a delay as compared to the formation of CO_2 , established by monitoring the exhaust of a reaction setup [22], which has led to the assumption that O_{elec} may be formed from O_β or O_{nucl} . The exchange rate between O_{nucl} and O_β is comparable to the rate at which molecular oxygen is adsorbed. If only step 4 in figure 4.3 is included in a simulation the delay is far greater than measured so step 3 must be included. The calculations showed that the rate of step 4 is twice as high as step 3, why O_{elec} is formed mainly from 3 in Ag catalysts that are not characterized by even surfaces. This prompts for TFY/RIXS measurements because the O_β species, that may govern the O_{elec} production rate, is located in the bulk, which is not reachable by the *in situ* XPS measurements.

Does un-dissociatively adsorbed molecular oxygen play a role in the epoxidation process? As it turned out our *in situ* measurements, along with project calculations, will re-open this, former highly debated, question. The consensus since the 1998 review [23] has been that molecular oxygen was of no significance - though under clear reservations with regard to the pressure gap issue of the experiments, UHV or below 10^{-4} mbar, from where this conclusion were

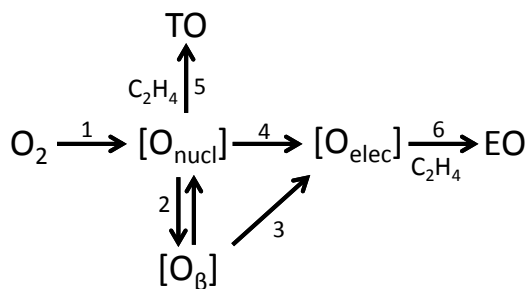


Figure 4.3. Oxygen transformations in Ag under reaction conditions. [] indicates atomic adsorbed oxygen. Step 1 is gaseous molecular oxygen that dissociatively adsorbs on the Ag surface to form O_{nucl} . Process 2 indicate a formation equilibrium between O_{nucl} and O_β . Step 3 shows the nucleophilic activation of a C–H bond in ethylene leading to total combustion. Step 3 and 4 indicates the origin of O_{elec} that in step 6 activates an ethylene C–C bond leading to epoxidation.

drawn. Moreover, we find that Ag–O–H groups forms during reaction and may have reaction influence, something that have not been considered before.

Considering the above, the objectives for my work on the ethylene epoxidation reaction has been the following:

- Develop a reaction cell
- Perform *in situ* XAS/RIXS measurements on the O K edge
- Characterize/Identify oxygen species

5. Results

In this chapter, the results of the papers and manuscripts of my thesis are summarized.

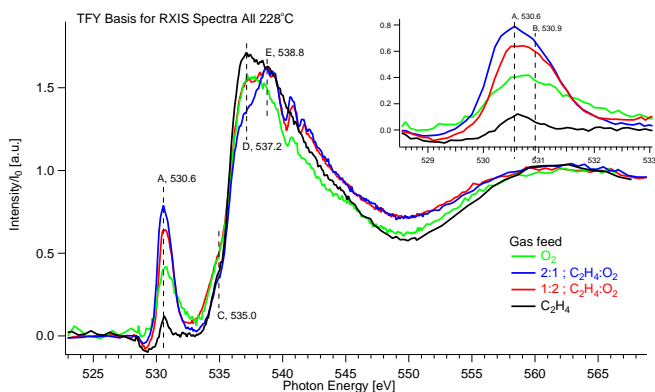
5.1 Ethylene epoxidation over Ag

A typical experimental procedure to study ethylene epoxidation over a Ag catalyst contains the following steps:

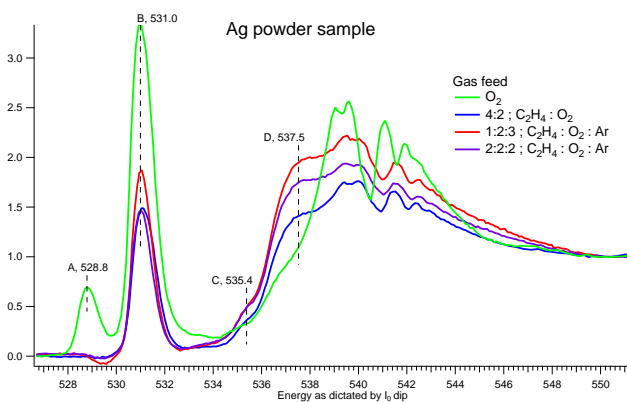
- A thin film of Ag is deposited onto a SiN membrane *or* a powder Ag sample was mounted on the membrane disk and either was inserted into the reaction cell system (see Fig. 3.6 above), and attached to the synchrotron radiation end station.
- “Oxygen loading” procedure: the Ag sample in the cell is heated to $\sim 225^\circ\text{C}$ in a pure 10 SCCM O_2 flow. These conditions are kept constant for several hours (at least 12 h) to allow the system to reach equilibrium.
- X-ray spectroscopy is performed at this stage.
- Reaction conditions: the temperature is kept constant at 225°C while the gas feed is changed to a reaction mixture, e.g. 5:5 SCCM ($\text{O}_2:\text{C}_2\text{H}_4$). X-ray spectroscopy is performed during the transition and when equilibrium is reached to investigate the dynamic development.
- Further changes to the mixing ratio of the gases are monitored by x-ray spectroscopy similarly as described in the above procedure.

Figure 5.1 shows *in situ* TFY data obtained either under a pure O_2 flow or a reaction mixture over (a) an Ag film and (b) Ag powder, respectively. The salient features at which the spectra differ are indicated by vertical dashed lines. The only data treatment done is a I_0 - and edge jump-normalization. These spectra clearly show that the develop *in situ* cell is capable of detecting feed conditioned changes of the oxygen present in the Ag during oxygen loading and between reaction mixtures.

The Ag film (Fig. 5.1(a)) has a larger gaseous O_2 contribution under reaction conditions. This is due to island formations of the initially 68 nm Ag film and/or oxygen depletion from the Ag as compared to the oxygen loading condition. The inset shows that the σ^* -resonance region consists of two



(a)



(b)

Figure 5.1. *In situ* TFY data of the O K-edge. (a) of an initially 68 nm thick Ag film and (b) of a powder Ag sample. The temperature for all measurements were $\sim 230^\circ\text{C}$ and the gas feed is given in the legend.

components, where we attribute the low (high) energy feature A to gas phase (adsorbed) molecular O_2 .

The Ag powder measurements in Fig. 5.1(b) shows an unexpected peak A at 528.8 eV under the oxygen loading conditions. This is likely due to AgO forming in the bulk (see RIXS reference spectra below). This feature is not visible in the TEY, meaning that AgO does not form on the surface. This is probably due to that the surface is more prone to reconstruct under oxygen loading conditions and thus making pure metallic conditions more favorable. When going to reaction conditions, the 528.8 eV peak disappears, meaning that also caused the bulk reconstructs. We attribute the 535.4 eV peak C to Ag–O–H groups (supported by calculations, presented below).

Evaluation of gaseous O₂ background in the XAS signals

In the powder set up the photons travel through a thin layer of gas path before probing the sample. While the TFY-mode O K-edge spectrum contains a substantial O₂ gas phase background signal, the O K-edge TEY signal shows very little background. Figure 5.2 shows O K-edge spectra from a powder sample containing absorbed oxygen in a Ar atmosphere, respectively a O₂ gas atmosphere. The spectra are recorded within 20 min. so that the absorbed oxygen signal is expected to be very similar. (In the Ag film setup, the behavior of the TFY and the TEY-mode spectra with respect to the O₂-contribution is very similar to the Ag powder setup.)

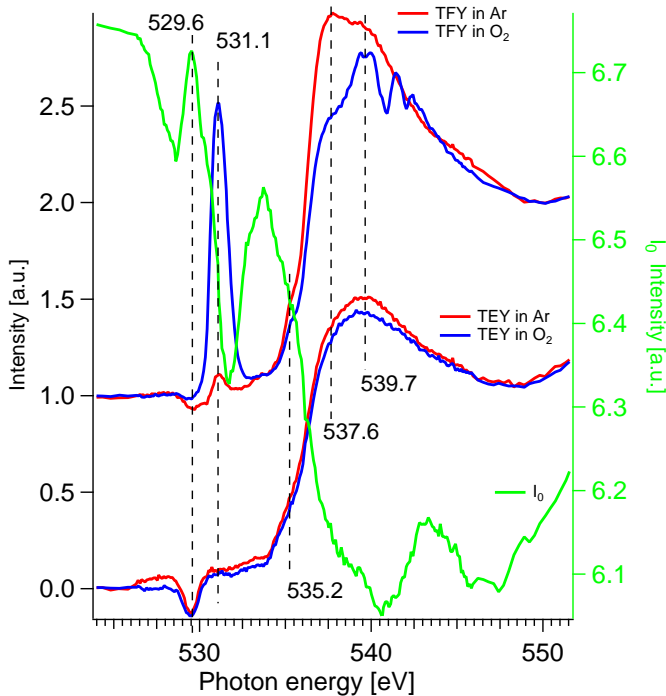


Figure 5.2. O K-edge XAS spectra (red and blue traces) from a Ag powder sample in different gas atmospheres as indicated in the legend. The top (blue and red) pair is TFY-mode XAS and the bottom pair is TEY-mode XAS. The green trace is the I₀-signal. The pre-edge dip (529.6 eV) is an artifact due to normalization by a contaminated I₀-signal. At the ALS the I₀ is obtained by an Au covered grid placed as the last beam interacting unit before the sample.

Fig. 5.3 shows that one can extract the O₂ gas phase signal by creating a weighted difference between the two TFY-mode spectra of Figure 5.2. The resulting gaseous molecular O₂ spectrum (black trace) closely resembles the one in reference [24]. In both cases saturation effects are less pronounced due to a thin probing layer in our case and a low gas pressure in the reference

spectrum. This procedure can be reversed with a thus obtained O₂-spectrum for extracting the evolution of Ag-absorbed oxygen species, which is demonstrated in Fig. 5.4.

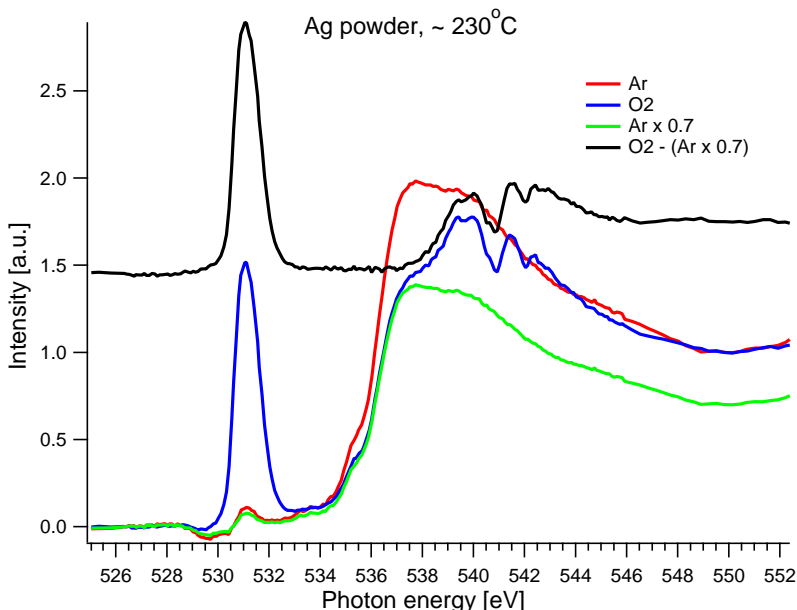


Figure 5.3. O K-edge TFY-mode spectra from a Ag powder sample in different gas atmospheres as indicated in the legend. The black trace is a difference spectrum for extracting the gas phase O₂ contribution.

By subtracting the previously extracted O₂ spectrum (black trace) from H (I(74.83,81.75)), the total signal of the oxygen species dissolved in the Ag appears under loading conditions (reaction conditions). If one instead subtracts the raw H spectrum from I(74.83,81.75), with a weighting factor that makes the Rydberg dips disappear, one obtains the relative difference to H. One observes that in the course of 5 h the two high energy features (dashed vertical lines) have gained intensity. The 1:1 reaction condition promotes the peak at 537.3 eV over one at 540 eV. Note that saturation effects are more pronounced on the σ^* -resonance. This explains the apparent deviation at this energy for the difference spectra of I(74.83).

This shows that certain absorbed oxygen species that exist after oxygen loading gradually increase when subjected to reaction conditions.

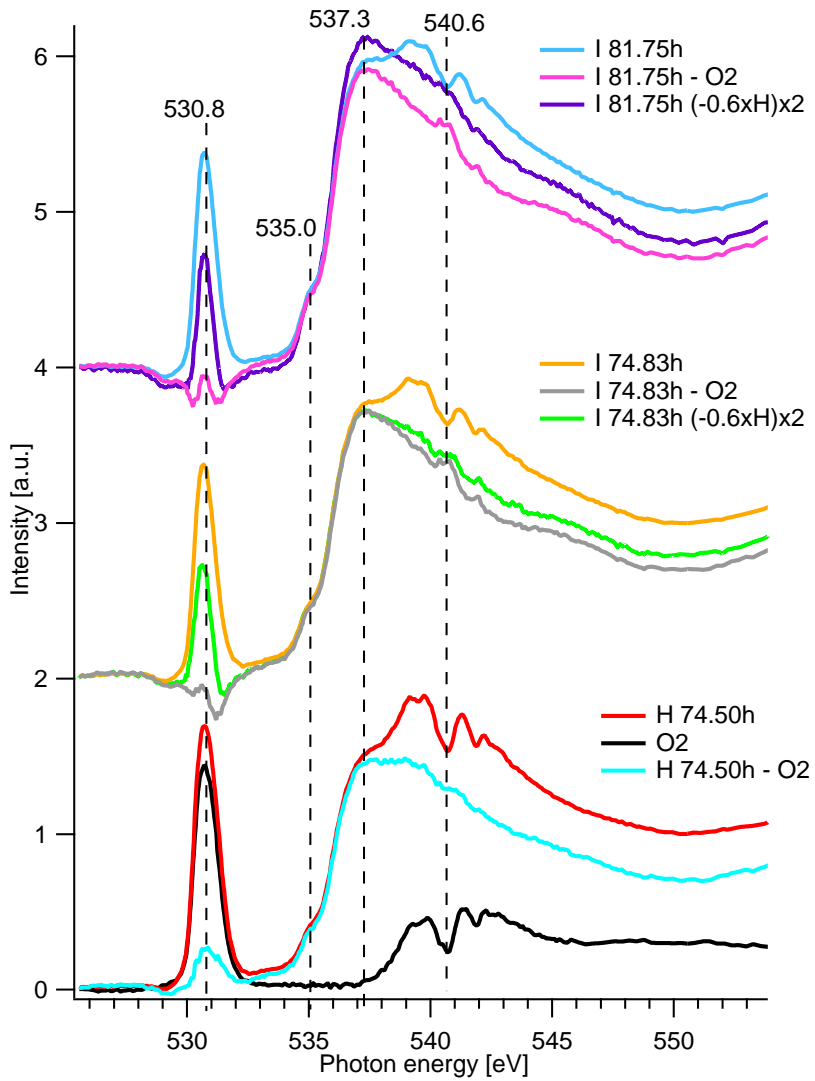


Figure 5.4. H denotes a pure O₂ feed and I denotes a 1:1 reaction mixture feed at two different later times (5 h apart).

Comparison to Ag oxides

A comparison of the XAS from active species (from Fig. 5.4) to those from silver oxide reference powder is seen in Fig. 5.5. No apparent similarities are seen, except for the 530.7 eV peak of Ag_2O that coincides with the gaseous σ^* resonance. The RIXS of Ag_2O and Ag_2CO_3 further confirms (Fig 5.6 (a) and (b) respectively) that none of these are formed, as they bare no resemblance to any of the *Ag in situ* RIXS spectra. However, the first XAS peak of AgO is close to the same energy of the unexpected XAS peak that appeared in the pristine, oxygen loaded Ag powder TFY-mode XAS. In Fig. 5.7 the comparison is explicitly done with both XAS and RIXS and it can here be concluded that the unexpected peak is AgO .

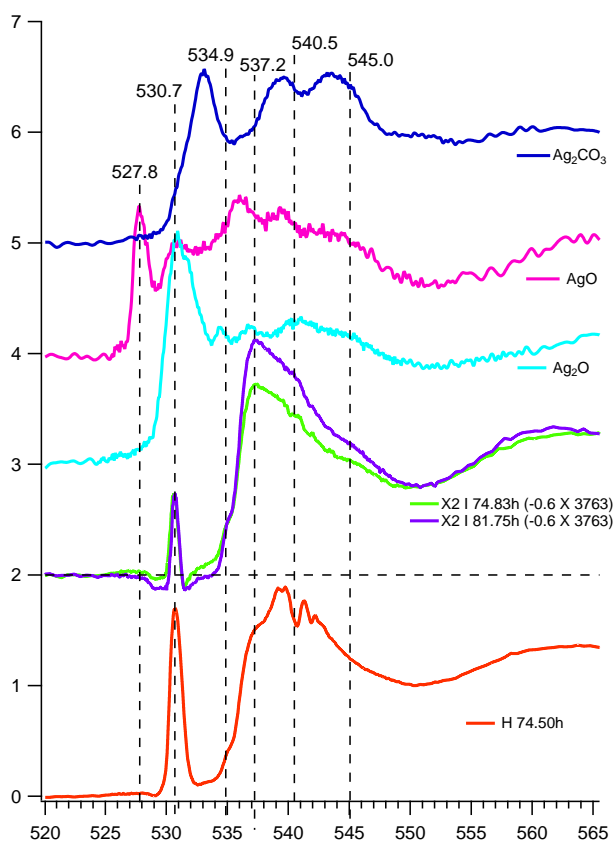


Figure 5.5. O K-edge XAS of several silver oxides (powder reference samples) compared to differenc spectra (fingerprints of active oxygen species) of Ag powder under different atmospheric conditions. H, Red trace: oxygen loading conditions. I, purple and green trace: reaction conditions for different length of exposure time.

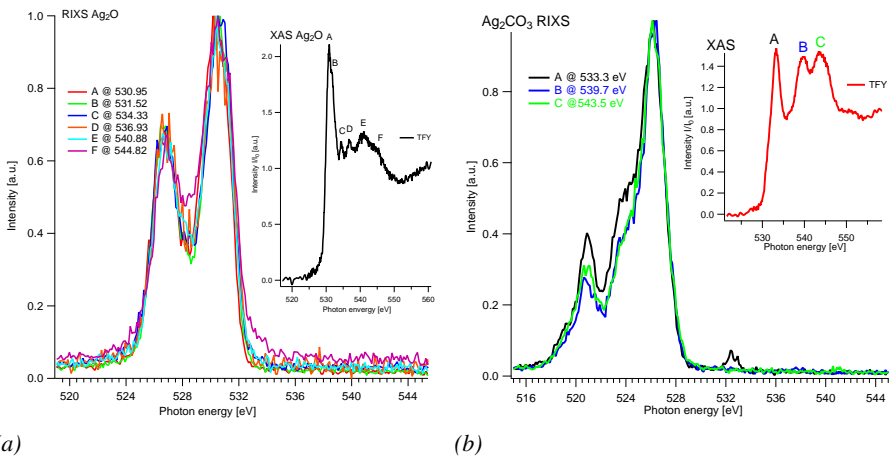


Figure 5.6. O K-edge XAS and RIXS of (a) Ag_2O and of (b) Ag_2CO_2 .

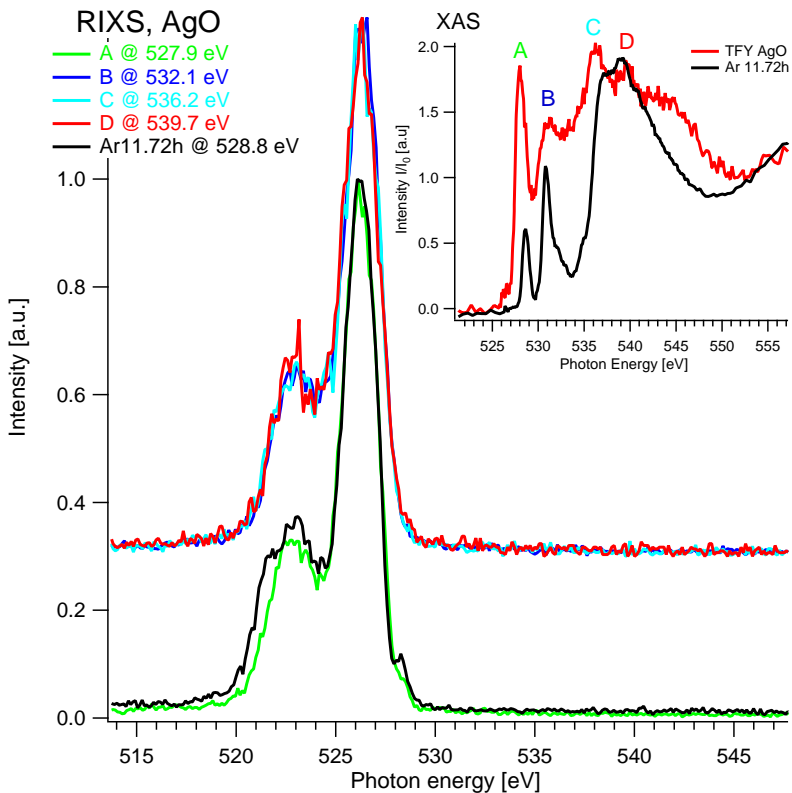


Figure 5.7. O K-edge XAS and RIXS of AgO and Ag powder in pure Ar.

Comparison to peroxides

In Fig. 5.8 the TFY of four peroxides are compared to the fingerprint of the oxygen species in Ag evolving under reaction conditions. As seen the one that come close is of meta-chloroperoxybenzoic acid (mCPBA), an organic compound shown in Fig. 5.9.

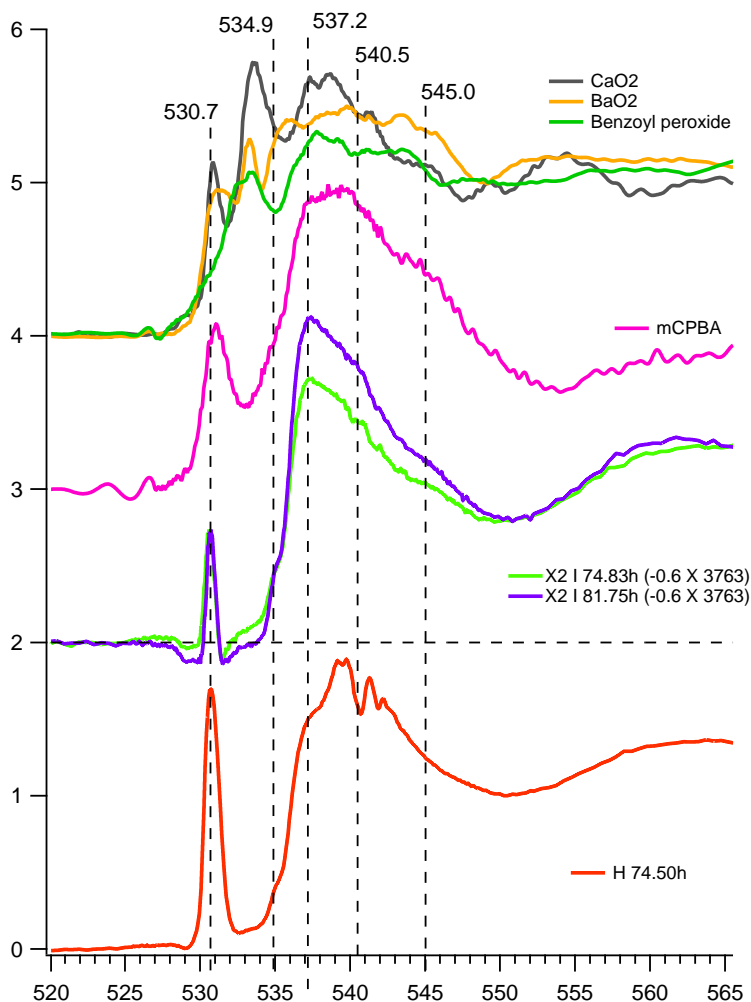


Figure 5.8. O K-edge XAS of four peroxides (powder reference samples) compared to difference spectra (fingerprints of active oxygen species) of Ag powder under different atmospheric conditions. H, Red trace: oxygen loading conditions. I, purple and green trace: reaction conditions for different length of exposure time.

The high degree of resemblance of the mCPBA- and the fingerprint-XAS indicates that the active species create multiple oxygen bonds (red sticks balls in Fig. 5.9).

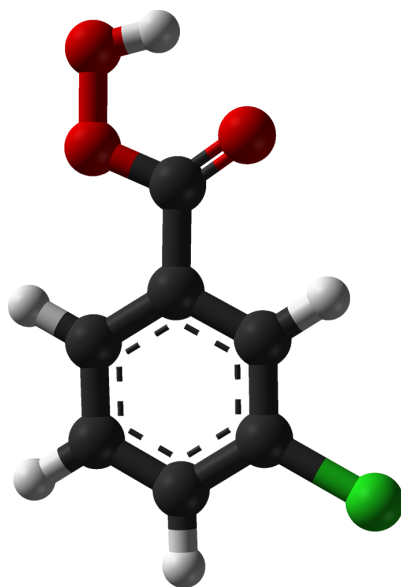


Figure 5.9. Stick and ball model of mCPBA. Black: C, Red: oxygen, Green: Cl, White: H.

XAS calculations of adsorbed oxygen species

In a collaborative effort, XAS calculations have been performed by Simone Piccinin¹ and Travis Jones² to simulate the ethylene epoxidation process over Ag at few mbar. Some possible explanations to the spectra we have recorded at $T \geq 180^\circ\text{C}$.

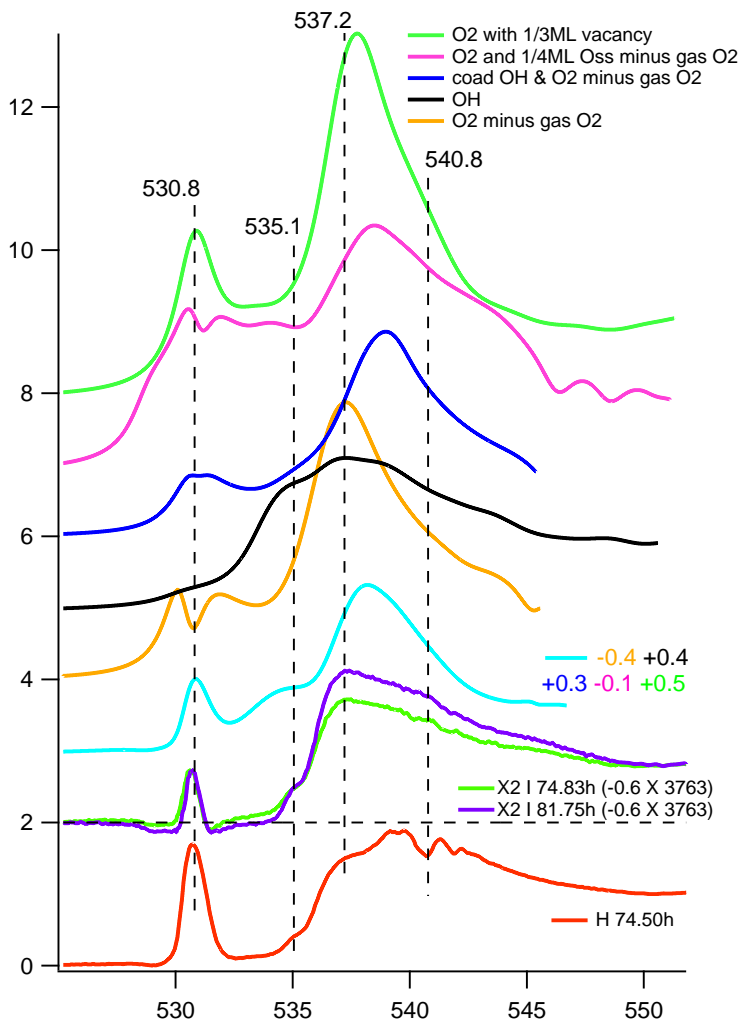


Figure 5.10. The identified active signature may well consist of a combination of several adsorbed species. A bid on a possible combination is given by the turquoise trace.

¹CNR-INFM DEMOCRITOS National Simulation Center, Theory@Elettra Group, Trieste, Italy

²CNR-IOM & FHI Berlin

In Fig. 5.10 some of the XAS spectra that Travis have calculated is shown along with the finger print of our active species. The bottom red trace and the active species fingerprints, in green and purple, are the same as in Fig. 5.8. The remaining spectra are all calculated.

The orange spectrum is of molecular O_2 chemisorbed on a regular Ag(111) surface. This species is unstable at reaction temperature, but can not be ruled out as a transient species or potentially stable at defect sites, in particular not in our 1 atm setup. The black trace is of adsorbed O–H which is thermodynamically stable under reaction conditions. The blue trace is of co-adsorbed O–H and O_2 which becomes favorable when the O–H coverage exceeds 1/4 mono layer, ML, and in which the O_2 adsorbs to an Ag top site and the upward pointing H. The pink trace is of subsurface oxygen, present at 1/4 ML in octahedral holes in the Ag(111) surface, with 1/4 ML O_2 adsorbed on the surface. In the pink spectrum the relative intensity of the pre 535 eV features are proportional to the amount of sub surface oxygen present. The green top trace is of O_2 adsorbed in surface vacancies, with a surface vacancy density of 1/3 ML where the O_2 molecules adsorb in the edges of the vacancy. This is a apparently high vacancy density, but adsorbed O–H and dissolved oxygen reduces the formation energy from 0.46 eV on a clean surface to 0.13 eV. By the calculation this molecular species may be present at temperatures up to 227°C, which would be the first example of such know to us.

The turquoise trace in Fig. 5.10 is an attempt to mimic the active signature by creating a linear combination of the five theoretical spectra. The relative weight (coefficients) of the different calculated spectra is indicated in a legend next to the turquoise spectrum. Negative values for a coefficient indicates that the corresponding oxygen species has a lower abundance under reaction conditions than under loading conditions.

Certain constraints to the coefficients are the following. The negative value of adsorbed O_2 (not at a vacancy) (orange trace) is justified by the high vacancy density at reaction conditions. There must be more adsorbed O–H due to the shoulder at 535 eV in the purple and green trace, which only is present in the black trace. This entails that there probably is also more co-adsorbed O–H and O_2 (blue trace). Other evidence indicates that some sub-surface oxygen (magenta trace) is consumed by the reaction, thus the negative coefficient. The low formation energy suggests a saturation of vacancies on the surface so that there will be an increase contribution of O_2 adsorption that is vacancy facilitated (green trace).

The calculation shows that if the surface vacancy concentrations is 1/4 ML then 1/4 ML O_2 adsorbs inside the surface vacancy. Increasing the surface vacancy concentration to 1/3 ML causes O_2 to adsorb at the edges of the vacancies. This causes the a shift of the O 2p-states further away from the Fermi level in the O_2 adsorbed in a 1/3 ML surface vacancy concentration (Fig. 5.11).

This could possible correspond to the shift of the adsorbed molecular oxygen 2p-states that we observe in the O K-edge RIXS spectra for different reaction mixture ratios (Fig. 5.12).

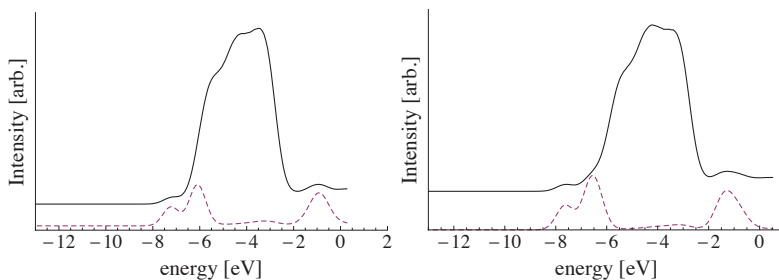


Figure 5.11. Black lines total DOS and dashed lines O 2p-states of adsorbed O₂ on a Ag surface at 1/4 ML vacancy concentration (left) and (right) 1/3 ML vacancy concentration (right). Work of Travis Jones.

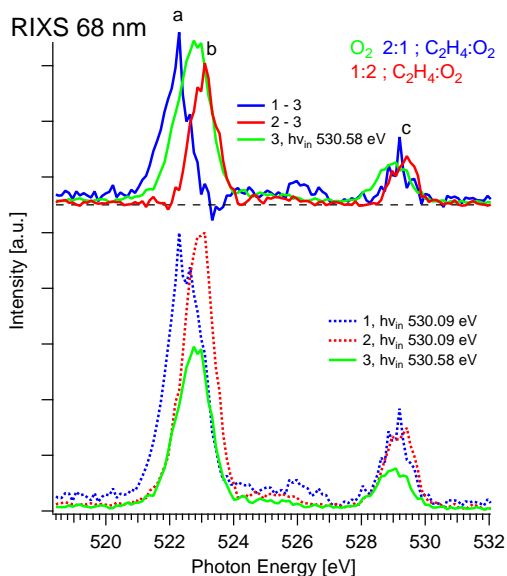


Figure 5.12. O K-edge RIXS of molecular adsorbed oxygen on Ag (initial 68 nm film) in different atmospheres. The incident photon energy has been chosen to be in the σ^* -resonance region.

Summary of results

The following list summarizes the main conclusions that can be derived from the *in situ* ethylene epoxidation over Ag results (Paper II).

- There are five distinct RIXS peaks, suggesting up to five oxygen species that are loaded into the Ag. Some of these pose as candidates for O_{elec} as their apparent abundance goes up as the EO production increases.
- Adsorbed molecular O_2 : The low energy peak in XAS (σ^* resonance) contains multiple components: gas- O_2 and adsorbed- O_2 about 0.36 eV apart. The inset of Fig. 5.1(a) shows these two components. Corresponding RIXS, Fig. 5.12, shows that a new spectrum emerges for excitation at close-lying energies indicating two different O_2 molecules, one free and one adsorbed. Depletion measurements show that the desorption of the assumed adsorbed molecular oxygen is a relatively rapid and monotonic, as expected for a surface adsorbed species.
- Ag-O-H groups: The main O K-XAS edge has a shoulder at about 535 eV when the Ag is exposed to reaction conditions (Fig. 5.1(b)). This we attributed to Ag-O-H groups. RIXS excited at this energy shows distinctly different spectra for pure O_2 and reaction mixes.

Outlook

It often takes several days until chemical equilibrium is reached in Ag under reaction conditions, which should be considered in future experiments.

The conversion and selectivity towards EO is found to be close to the limit for the gas reaction product detection (gas chromatograph and quadrupole mass spectrometer). The implementation of a sniffer-like setup would offer a more sensitive way to monitor the conversion rate. This entails that a capillary, with its opening close to the probed spot on the sample, is connected to the gas analysis equipment (see further below in Fig. 5.16).

The used Ag film thicknesses, ranging from 14 to 68 nm, yields TFY-mode XAS spectra where the gaseous O_2 contributions are considerable. Using thicker Ag films, e.g. 100 nm, could provide less "contaminated" spectra and as a bonus a thicker Ag film may provide enough heat conduction to hinder island formation.

An inherent problem with the film setup is the inability to, in a reliable manner, measure the actual temperature of the sample. One way of getting closer to doing this could be to implement a thermocouple on the vacuum side of the membrane, see figure 5.13. In order to facilitate easy deposition the used metals should be pure elements, then the same evaporation setup that is used

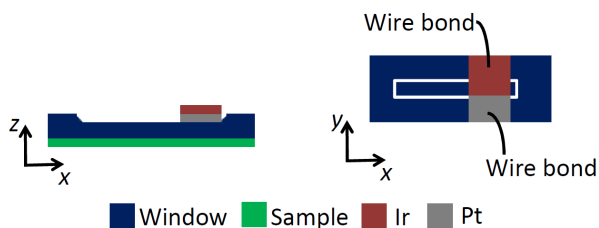


Figure 5.13. Possible way of implementing a IrPt thermocouple for the film setup. The white rectangle in the yx sketch marks the slope of the Si support frame around the Si_3N_4 membrane.

to deposit the Ag sample could be used. Thin films of Ir and Pt have proven to work well up to 800°C [25].

On a side note; It could be an interesting test to make a thermocouple as the suggested, though as thin as possible in the x -direction, and then let the beam penetrate the membrane at various angles, energies and intensities while tracking the temperature. This could be done with vacuum on both sides of the membrane or with the *in situ* cell. In the cell the effects of sample thickness, or no sample, as well as of the carrier gases could (or perhaps ought to) be measured. For instance, it could be relevant to test whether it makes a difference that He is used as a diluting carrying gas instead of Ar, 0.142 vs 0.016 $\text{W}/(\text{m}\cdot\text{K})$, with its nine times higher heat conductivity.

The powder setup offers the possibility of using so called promoted samples, meaning that elements are added to the Ag, or the gas feed, which are found to increase the selectivity. Cu is such promoter [26, 27] and the relatively high energy of the Cu L-edge makes it a good candidate for investigations.

5.2 RIXS studies of CO₂ and C₂H₄O

Measurements of the desired product, EO, from ethylene epoxidation and one of the total ethylene oxidation products, CO₂, were conducted to determine whether these contributed to the obtained *in situ* spectra - they do not, but these gas measurements turned out to have value in their own right.

RIXS measurements on CO₂ showed an unexpectedly large incident energy dependence in the 536-537.5 eV region which resulted in a cooperation with a theoretical group around Dimitrios Maganas from the Max-Planck Institute for Chemical Energy Conversion and Serena DeBeer from the Max-Planck Institute for Chemical Energy Conversion & Department of Chemistry and Chemical Biology, Cornell University, leading to Paper V.

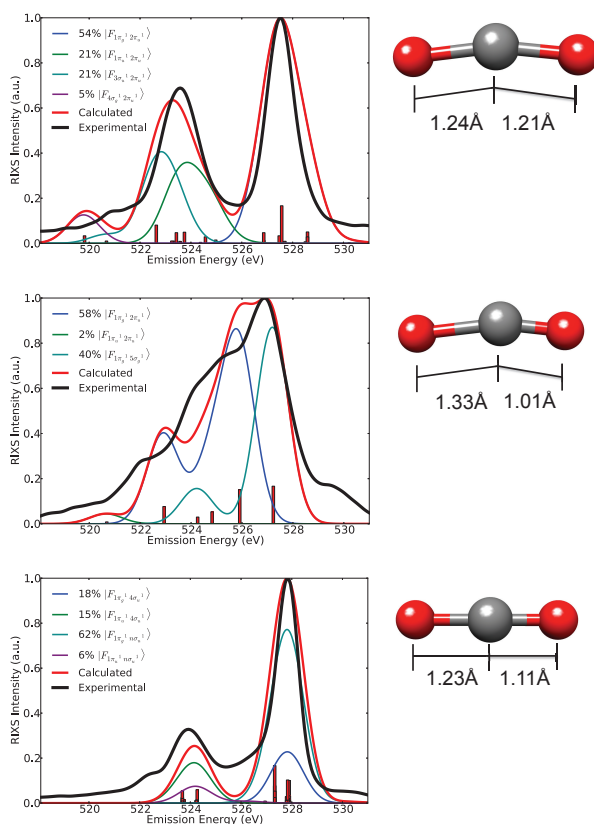


Figure 5.14. Experimental (black line), versus calculated MRCI/CISD (red line) RIXS spectra. The experimental spectra were taken at incident energies 535 eV (top) and 536.5 eV (middle) and 538.0 eV (bottom).

In order to interpret the experimental data, ab initio calculations at the level of multireference configuration interaction were performed and potential energy

surfaces along the dominant bending and antisymmetric stretching vibrational modes were constructed. The instability of the x-ray absorption reached intermediate states was interpreted by considering vibronic coupling between intermediate states and vibrational modes of proper symmetry. The Renner Teller and the core hole localization pseudo Jahn Teller effects couple the $|\Pi_u\rangle$ and the $n|\Sigma_{g,u}^+\rangle$ symmetric core excited states with the bending vibrational and the antisymmetric stretching vibrational modes, respectively. The RIXS spectra were evaluated along the corresponding predominant vibrational modes resulting in excellent agreement between theory and experiment.

Figure 5.14 shows a comparison of experimental and calculated O K-edge RIXS spectra. The calculations are performed for certain asymmetric oxygen-core excited molecular states of CO₂: $|\Pi_u\rangle$ (top), $1|\Sigma_g^+\rangle$ (middle), and $n|\Sigma_g^+\rangle$ ($n > 2$) (bottom), i.e. intermediate states reached by x-ray absorption. The red sticks are possible final states into which the core hole state decays. The corresponding molecular geometry is visualized as a stick and ball model to the right. The weight percentage for the deconvolution of the experimental RIXS is given in the legend. The thin colored traces are the corresponding broadened theoretical spectra. The thick black traces are smoothed experimental RIXS spectra excited at three different incident energies. The observed RIXS spectrum for resonant energies between 533-535 eV corresponds to a bent molecule. For incident energies ranging between 535-537 eV the observed RIXS spectrum corresponds to a highly distorted structure along both stretching and bending pathways. For higher resonant energies, the RIXS spectrum indicates a linear molecule that is only slightly stretched.

The measurements obtained from EO are displayed in Fig. 5.15 and are the subject of on-going theoretical work. The most conspicuous observation is a resonantly enhanced feature at scattered photon energy of 524 eV. This occurs for a narrow range of incident energy around 533.2 eV (close to the dip in the TFY seen in the inset).

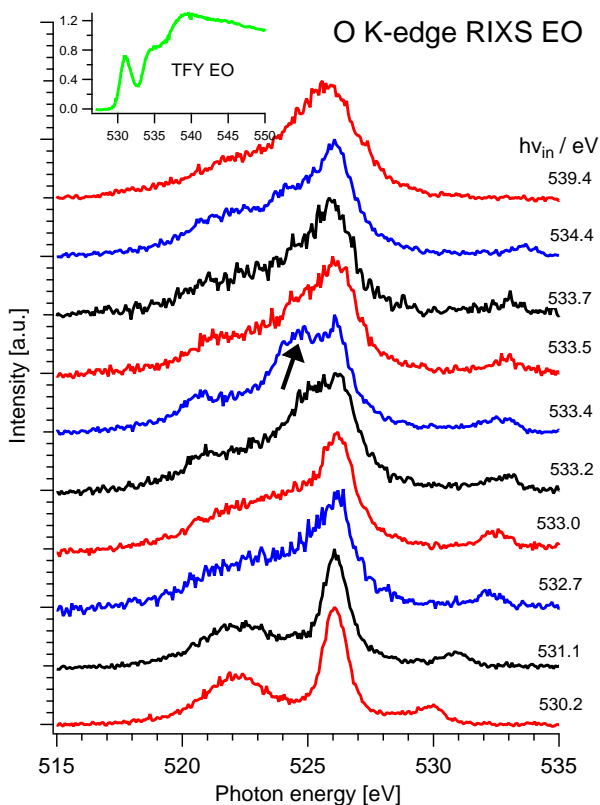


Figure 5.15. Incident energy dependent O K-edge RIXS spectra of EO at 1 atm pressure. Inset: O K-edge TFY.

5.3 Photocatalytic transition metal oxide films

Nanoporous WO_3

In this project the starting idea was to do an *in situ* investigation of the UV-activated catalytic decomposition of organic molecules on the surface of nanoporous WO_3 . It is found likely that electronic states in the band gap or surface electronic states contribute to the measured photo-reactivity of the nanoporous WO_3 [28, 29]. These are states where RIXS excels as a probe.

One long term goal of the WO_3 project is to be able to clean polluted water with sunlight as the only energy supply. Along with the photocatalytic properties WO_3 also exhibits electrochromic characteristics [30], that in future measurements could be investigated by applying a potential to the sample holder in the modified *in situ* cell, see figure 5.16.

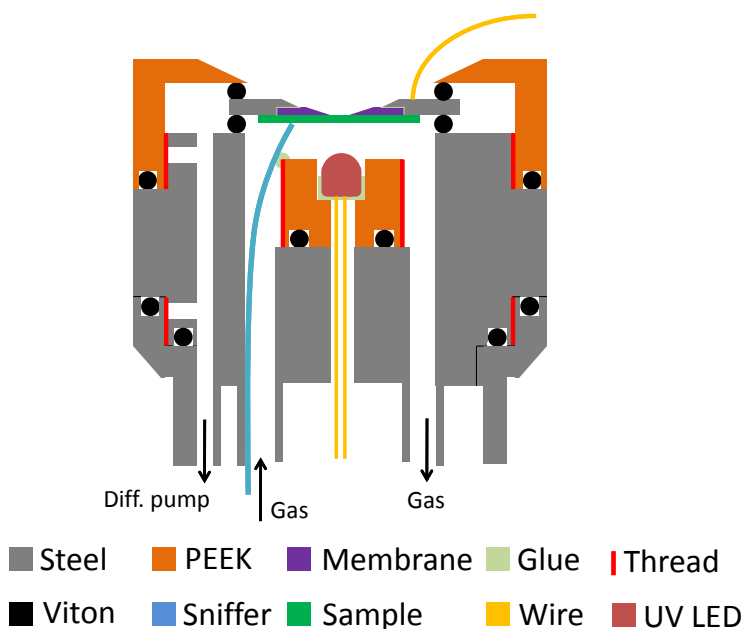


Figure 5.16. WO_3/TiO_2 *in situ* cell with UV-LED and a sniffer going to a mass spectrometer vacuum.

Figure 5.16 gives a schematic representation of the reaction cell developed on the basis of the epoxidation reaction cell described above. The two new features are that the center PEEK part includes a 10 mW UV LED (red) and a sniffer (blue line). The sniffer is used to probe the gas composition in the immediate vicinity of the active sample, where the concentration of the reaction products is only minimally diluted by the part of the inlet gas that does not get into contact with the sample. The used sniffer was an uncoated

silica capillary, 0.1 mm inner diameter and ~ 8 m long, which is commercially available for gas chromatographs. One end of the capillary was fixed in such a way that it terminated about 1 mm away from the Si_3N_4 membrane. The capillary is placed inside the inlet gas tube and leads to ambient air via a soft graphite ferrule feed through at the end of the manipulator rod (Fig. 3.5). From ambient the capillary leads into a mass spectrometer (MS) vacuum chamber, also sealed with a soft graphite ferrule, and the other end was positioned close to the MS filament. In this way the MS vacuum sucks gas from the active region of the cell and the MS vacuum can be varied by using different lengths of capillaries or controlling the temperature of the capillary.

The nanoporous WO_3 samples were deposited directly onto the Si_3N_4 membrane by reactive DC magnetron sputtering at 200 W, in a O_2/Ar ratio of 0.43 and with a substrate (the membrane) temperature of 280°C by the the division of Solid State Physics at UU.

In order to determine the conversion of the nano porous WO_3 offline tests were performed together with Martin Putnik, an exchange student from the University of Konstanz in Germany. The offline setup is displayed in figure 5.17. The reaction chamber was either equipment with a internal UV led, NS370L-5CLA, with a 1 mW maxium at 370 nm, 3.3 eV, that could be put in the direct vicinity of the sample (as with the reaction cell) or an external 300 W Xe arc lamp, Thermo Oriel lamp n. 6258, that would shine onto the sample through a UV-transparent window. The used test mixes were ethylene and oxygen in various ratios. Both flow modes and closed batch mode were tested. The volume of the closed test setup was about 25 ccm. The WO_3 test samples were produced on glass substrates in the manner described in article VIII and had a macroscopic surface area of about 4 cm^2 . The MS used to detect reaction products was a QMS 200 M with C-SEM from Pfeiffer Vacuum, the same as used in the ethylene epoxidation project.

Contrary to expectations [29], no evidence of conversion, meaning a production of H_2O and CO_2 , could be detected with WO_3 samples. Not even with the 300 W Xe arc lamp in closed batch mode. Therefore, more reactive TiO_2 samples were prepared on glass substrates as described in [31]. In brief; The TiO_2 films are deposited by dropping a solution containing TiO_2 particles and then dry the solvent away by heat. The activity of such a film is shown in figure 5.18, in closed batch mode with a 1:3 mixture of ethylene and oxygen and illuminated with the 300 W Xe arc lamp. By mass 44 it is clearly seen that there is CO_2 production when the UV-source on. Based upon the offline conversion tests, membranes with both WO_3 and TiO_2 samples were prepared for *in situ* measurements.

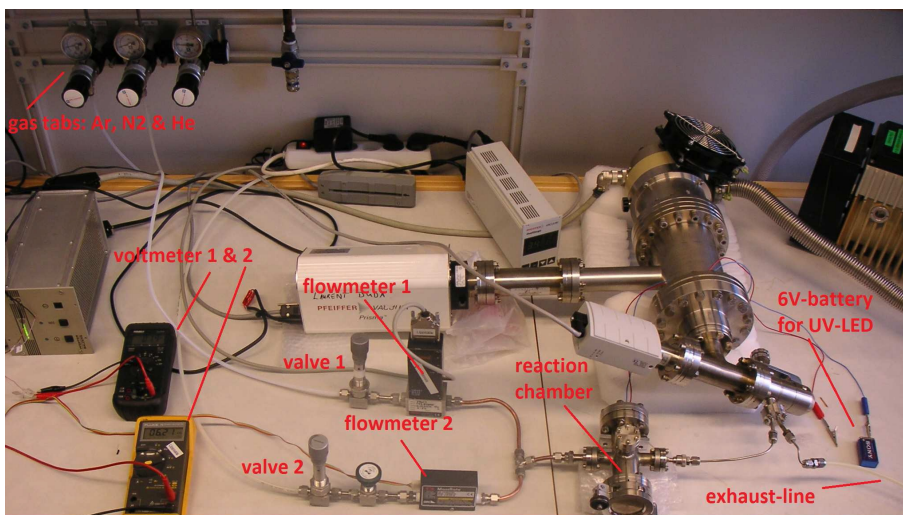


Figure 5.17. Picture of the offline conversion test setup for WO₃ and TiO₂ samples.

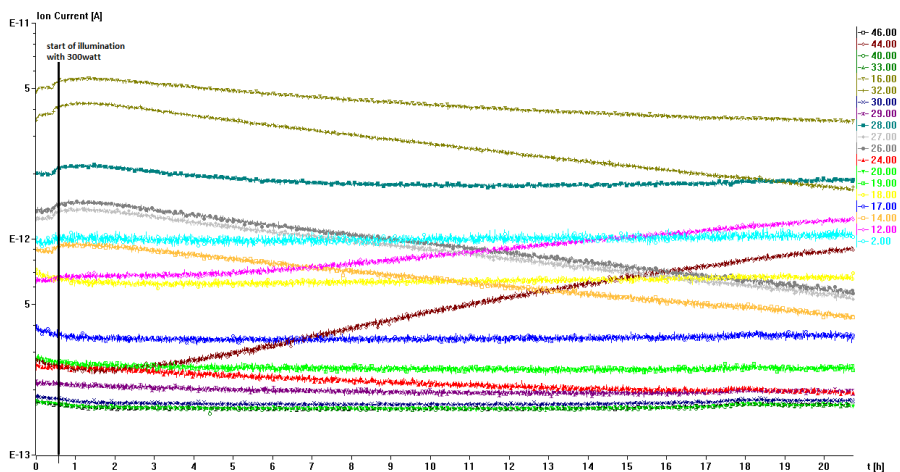


Figure 5.18. QMS data of the an active TiO₂ film. The general rise of the dominate masses after the UV light had been switched on is due to a heating of the reaction chamber due to the 300 W source. (data on crashed hard disk - cant make igor)

Ex situ and *in situ* WO₃

The interest in nanoporous tungsten trioxide (WO₃) is based on its many important technological applications, including chromogenics, photocatalysis, light emitting devices, sensors and batteries. Of particular interest is the influence of oxygen vacancies on its electronic and optical properties. Substoichiometric WO_{3-x} can contribute to localized states in the band gap. The existence of sub-band gap states in WO₃ is well-known, but the origin and implications of them for the optical properties are still not fully resolved. Several studies report on the blue luminescent emission from nanostructured WO₃ extending up to 550 nm, but consistent characterization of the band gap states responsible for this emission is by and large lacking. WO₃ is composed of corner sharing octahedral units. Different WO₃ phases owe their properties to the tilt and distortion of the octahedral units (second order Jahn-Teller effect).

Some interesting results came from *ex situ* measurements on WO₃ samples prepared under a partial pressure of either 10 or 30 mTorr of O₂, which are reported in Paper VIII.

The first attempt to perform *in situ* measurements were made on a ~50 nm WO₃ film. However, it turned out that the samples should be substantially thicker because the signal from gaseous O₂ was overwhelmingly dominant. Using the absorption cross sections from [8] an effective path length of 141 nm in a bulk like WO₃ sample would only transmit ~6% around the O K-edge. This means that the density of the deposited porous film is much lower than for bulk WO₃.

The x-ray spectroscopy experiments were performed on a ~100 nm WO₃ using a gas cell with a stationary atmosphere of ambient air (because the gas feed setup was not available at the time). In the anticipation that there would be "native" carbonates on the surface of the sample it was tried to turn the UV diode on and off in the search of differences in the electronic structure (Fig. 5.19). Small dependences of the UV illumination were found in the TFY measurements. The spectral intensity was generally enhanced when UV-irradiation was present. Moreover, we observe that the gaseous O₂- and the WO₃-contributions to the spectrum have contributions in the same order of magnitude at some locations on the membrane. Here the film has a suitable thickness for use on BESSY beamline U41-PGM. However, the WO₃ sample does not have an uniform thickness or porosity, as the different spots shows different intensity of the Rydberg dips (around 541 eV). Nevertheless, it could be interesting to test a considerable thicker sample e.g. 300 nm because the porosity of the material should allow activity deep below the surface.

In the purple trace of Fig. 5.19 the gaseous O₂ contribution has been removed. The resulting *in situ* spectrum is compared to the *ex situ* spectrum, showing an overall agreement with some differences in detail. The σ^* -resonance region could be artificially affected by saturation effects in the gas spectrum.

Simultaneously recorded TEY-mode spectra are presented in figure 5.20. Surprisingly, the spectra are very different from the TFY-mode spectra but also here there is an analogous intensity tendency as in the TFY, in particular at specific energies, marked a and b. One must keep in mind that the samples have a high resistivity and therefore drain current measurements are difficult. Moreover, the refocusing mirror is heavily oxygen contaminated (which thus provides an artificial I_0 reference) adds to the uncertainty of whether the differences, marked with a and b, are reliable. A further complication of TEY measurements on WO_3 is the non-conductivity of the material, which appears to lead to severe charging effects that causes the measured profiles to largely follow the I_0 structure.

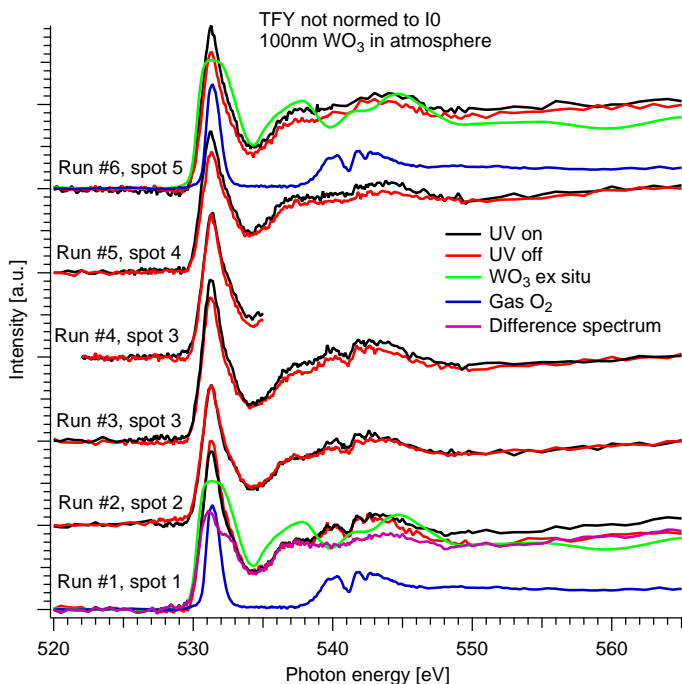


Figure 5.19. *In situ* O K-edge TFY spectra of a ~ 100 nm thick WO₃ sample in ambient air.

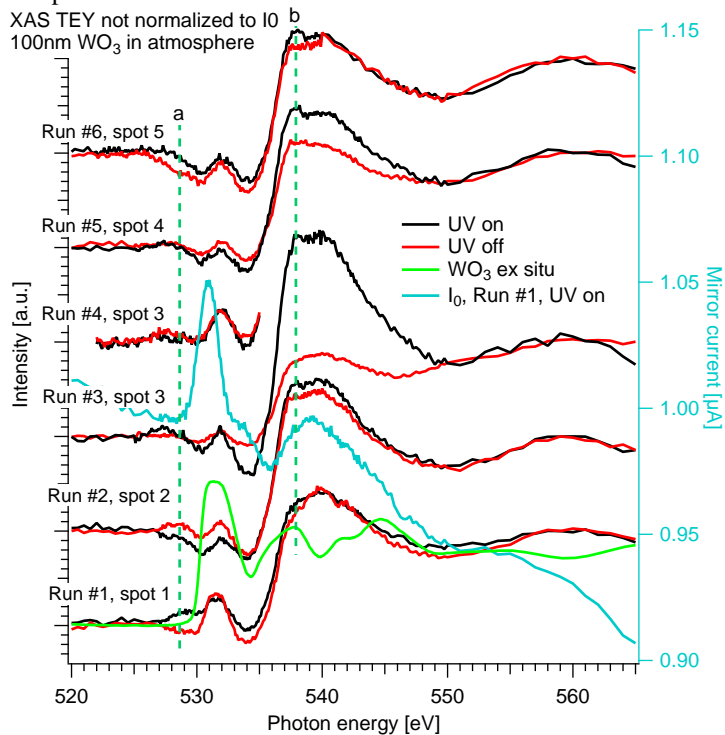


Figure 5.20. *In situ* O K-edge TEY spectra of a ~ 100 nm thick WO₃ sample in ambient air.

TiO₂ *in situ* measurements

The *in situ* measurements were conducted with a flow of 3:3 SCCM ; O₂:C₂H₄ and the illumination was done by LED with a 10 mW output at 370 nm. The gas diagnostics consisted of a QMS and the conversion was not sufficient for a detection. The performed *in situ* measurements on TiO₂ are displayed in figure 5.21, 5.22 and 5.23.

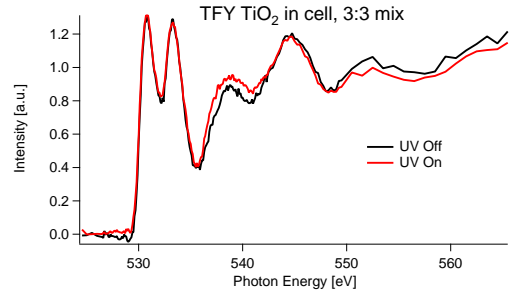


Figure 5.21. *In situ* O K-edge TFY measurements of a TiO₂ sample.

The measurements marked as ex situ (green traces) were done on the same samples as the *in situ* measurements just with the sample side facing against the beam, meaning that the beam did not go through the membrane.

As seen no impact on the electronic structure is detected by the *in situ* measurements. This could be due to too thick TiO₂ films, as the deposition method did not offer a good control of the final sample thickness.

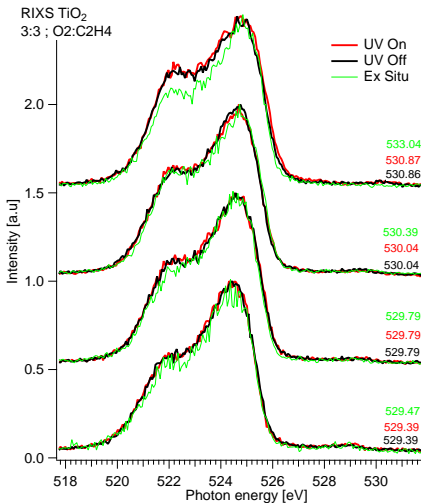


Figure 5.22. *In situ* RIXS measurements of a TiO₂ sample on the O K edge. The colored numbers on the right indicates the excitation energies.

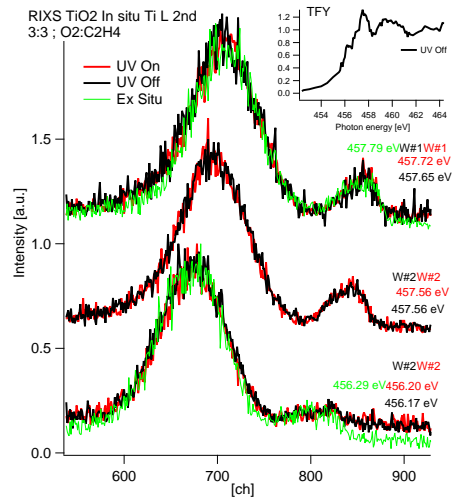


Figure 5.23. *In situ* RIXS measurements of a TiO₂ sample on the Ti-L edge. Note that the *x*-axis is the channel number and not an energy scale.

5.4 Water splitting with precious metal oxides

In this project the intention was to do *in situ* measurements of water oxidation on a Pt surface. A cell was developed to facilitate such measurements, see figure 5.24 and the end of paper I.

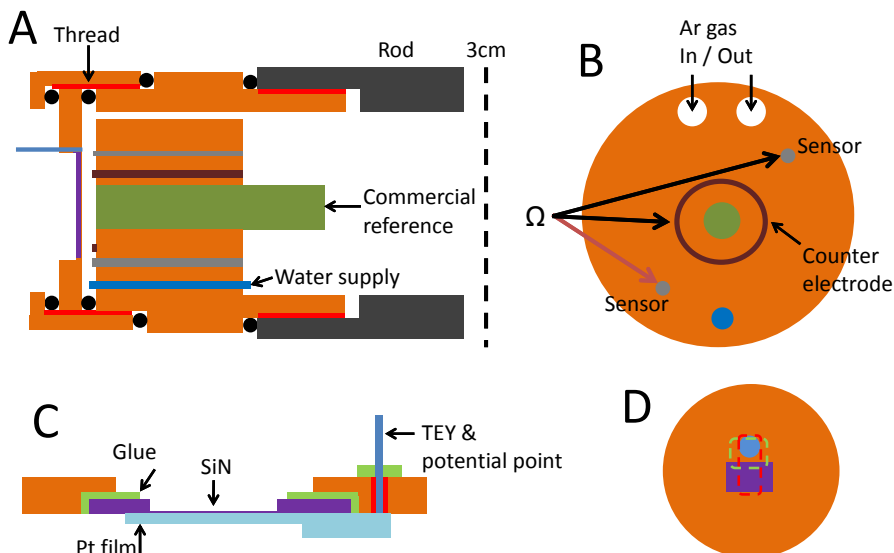


Figure 5.24. Water oxidizing *in situ* cell. Orange parts are of PEEK. A is a side way cut showing the entire cell screwed onto the rod. B is the cell seen head on without a cap. C is a side way cut of the cap. D is a bottom view of the cap indicating how the sample is deposited by the use of two masks.

The functionality of the cell goes as follow: It is a three electrode setup where the active sample (in this case a Pt film) is the working electrode. The counter electrode consists of an Au ring (formed of a \varnothing 1 mm solid Au wire) that encircles a Ag/AgCl reference electrode from Gaskatel [32]. The Pt sample is evaporated onto the cell cap holding the Si_3N_4 membrane and the electric contact, which was created by use of two masks: Mask 1 is used to deposit a relatively thick layer that connects the electric contact and the membrane support. Mask 2 is then used to deposit the part of the sample that covers the membrane and connects the membrane area with the external electric contact.

During reaction the cell is filled with liquid by a channel at the bottom of the cell (blue line and circle in Fig. 5.24 A and B). The liquid supply channel is drilled with two different diameters: from the backside, meaning the end screwed onto the rod, and about 2/5 of the way through a \varnothing 2.5 mm drill was used, big enough to make a threaded coupling to the plastic hose going to the syringe, and from the front side a \varnothing 1 mm was used, as the amount of water going to the vacuum, in case of a membrane failure, is the reaction volume plus

the amount evaporating from the supply that in turn is proportional the area of the supply source. The liquid reservoir is a syringe, connected to the liquid channel by a plastic hose, whose freedom should be restricted, as a membrane failure otherwise would suck it empty.

Since PEEK is hydrophobic [33] capillary effects are not present. This facilitates that the water level can be detected by measuring the resistance between the sensors and the counter electrode marked in the B part of figure 5.24. The end parts of the sensors, that are in contact with the liquid, are of Au. The advantage of being able to vary the water level below the membrane area is, that it allows for measurements between in the *in situ* ones where the signal originating from water is minimal.

To carry the reaction products to a gas analyzing instruments, and to allow for a changing water level with a minimal change of the pressure difference over the membrane, an inert gas volume is kept at constant pressure above the water level. As in the case of the epoxidation cell the gas tubes were fit with security solenoid valves connected to the end station interlock system. The top water level sensor is here utilized to ensure that the reaction volume does not overflow.

In figure 5.25 a TFY measurement of the O K-edge of a nominally 70 nm thick Pt film with water in the reaction volume is displayed together with a pure water spectrum from [34]. Probably the Pt thickness was much less than 70 nm because the membrane area was translucent. Based on an effective x-ray path length of 200 nm, one would expect that less than 1% of the x-rays are transmitted at the O K-edge by using the absorption cross section values of [8]. However, the signal to noise ratio of the displayed spectrum is much greater than this implies. Membrane failure prevented further experiments.

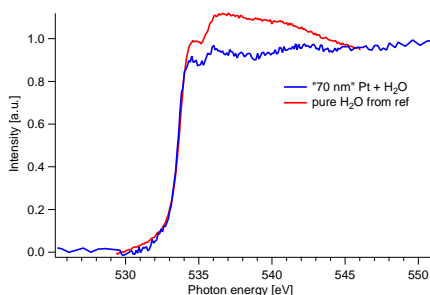


Figure 5.25. TFY O K edge spectrum obtained with a supposedly 70 nm Pt film. A spectrum of pure H₂O, from [34], is included for comparison. The H₂O reference have been shifted -0.8 eV.

5.5 Li-ion batteries

5.5.1 Introduction

Rechargeable lithium-ion batteries, already widely in use in portable electronic devices, are now envisioned to power more demanding applications, such as electric vehicles. In order to take this step, it is crucial to further improve key properties of these rechargeable lithium-ion batteries, such as capacity, rate capability, cycle life, among other things. To contribute to this goal, most investigations are directed at the improvement of cathode materials [35].

Papers III and IV are studies of the first charge/discharge cycle for the battery electrode materials, in order to achieve in-depth understanding for the origin of its capacity loss upon cycling. We apply a powerful combination of *ex situ* techniques: x-ray diffraction, soft x-ray absorption spectroscopy (XAS) and resonant inelastic X-ray scattering (RIXS).

5.5.2 The anode material $\text{Li}_x\text{Ni}_{0.5}\text{TiOPO}_4/\text{C}$

The work presented in this sections highlights the main insight of Paper IV: It is found that the amorphous phase that is formed from the anode during the first cycle is the active component of the battery and not the initial crystalline phase. *In situ* x-ray diffraction measurements have shown that the material becomes amorphous and therefore this state must be active one in the subsequent lithiation/delithiation battery cycling. This is corroborated by the behavior of the partial fluorescence yield (PFY) of the O K-edge peak energies. It is also argued that the initial $\text{Ni}_{0.5}\text{TiOPO}_4$ crystal structure forms a new crystalline oxide before becoming amorphous.

Figure 5.26 shows the PFY intensity at the O K-edge XAS peaks, meaning the resonant energies characteristic of the initial crystalline material, as the anode is going through its first cycle. As the cross sections for the four peaks energies generally goes up as the anode is lithiated and goes down when the anode is de-lithiated it seems that the O in the initial crystal behaves directly opposite of what one would expect if it is assumed that the rigid band model applies. That the cross sections goes down from the pristine sample to $\text{Li}_{0.5}\text{Ni}_{0.5}\text{TiOPO}_4/\text{C}$ could be due to that this stages' moderate lithiation is not sufficient to initialize amorphization.

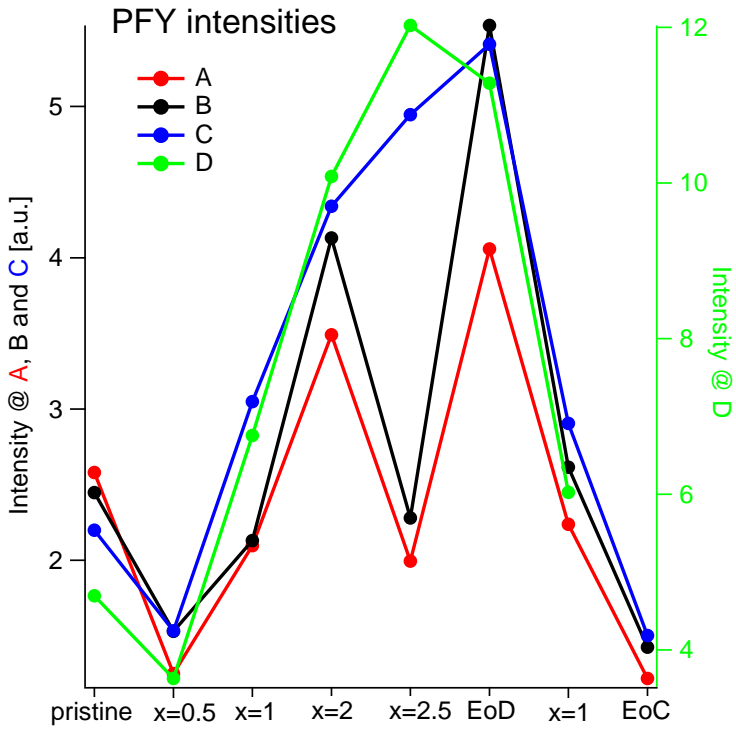


Figure 5.26. PFY intensities at the O K-edge XAS peak energies. The x's indicate the lithiation level. EoD is end of discharge and EoC is end of charge. A–D represent increasing XAS O K-edge peak energies.

5.5.3 The cathode material $\text{Li}_{2-x}\text{MnSiO}_4$

The Li-ion cathode material $\text{Li}_{2-x}\text{MnSiO}_4$ is the subject of paper III where measurements are done on samples stopped at various potentials during the first charging cycle.

It is found that a valance change of Mn from +3 to +4 is associated with a loss of the long range order of the crystal structure and that during the first part of the charging process the extraction of lithium ions is not accompanied by a change in the electronic structure of the expected redox active Mn atom but rather by a change of the electronic structure of the Si–O network.

Not included in the article is the Mn L-edge TFY data displayed in figure 5.27 that exhibits nearly perfect reversibility, even better than the M L-edge TEY data suggest. This supports that the effects of the ESI formation is more pronounced in the surface region.

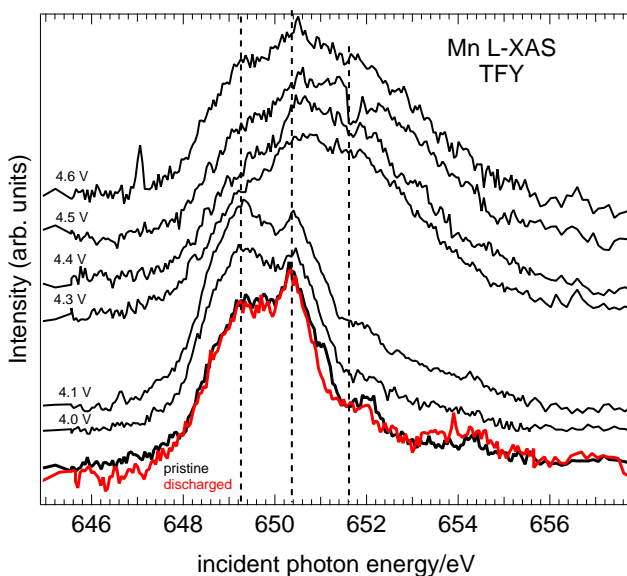


Figure 5.27. Mn L_3 -edge TFY-mode spectra of $\text{Li}_{2-x}\text{MnSiO}_4$. Red trace is the spectrum of the discharged sample superposed onto the spectrum from the pristine material showing a high degree of reversibility of the Mn oxidation state.

5.6 Sulfidation of natural Cu oxides

Only certain Cu oxides form naturally on Cu metal, namely cuprite, malachite, tenorite and paratacamite. The sulfidation of such oxides grown on Cu substrates is studied in paper VI. This project is subject of paper VI, a continuation of a project initiated earlier [36]. It is concluded that the main mechanism for reduction of Cu(II) sulfidation of corrosion products on copper is the disproportionation reaction $\text{Cu}^{2+} + \text{Cu} \rightarrow 2\text{Cu}^+$. This is manifested by the fact that the powders only slightly change in spectral shape, while the oxides on the Cu substrates were strongly affected by the sulfidation, as seen in Fig. 5.28.

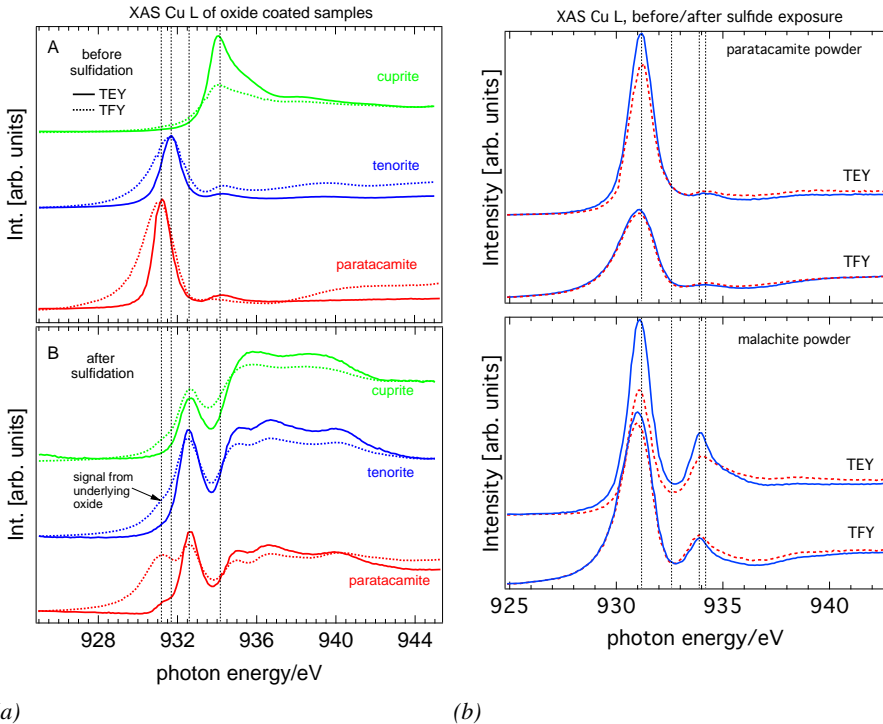


Figure 5.28. (a) Cu L-edge of oxide-coated Cu samples before and after sulfidation. (b) Cu L_3 -edge of pure oxide powders before and after sulfidation.

6. Conclusions and Outlook

In this thesis I have reported on the design, construction, and application of a novel reaction cell for heterogeneous catalysis experiments. I demonstrated how to extract information about transient oxide species in Ag during ethylene epoxidation performed at $T=230^{\circ}\text{C}$ and $P=1\text{ atm}$. Important new insights are that adsorbed molecule oxygen is present and that Ag–O–H groups form under reaction conditions. It is possible to do *in situ* XAS and RIXS O K-edge measurements of the ethylene epoxidation process over Ag!

Promoted ethylene epoxidation experiments can readily be accommodated with the above developments. Furthermore, the reaction cell can easily be modified for photocatalytic and electrochemical applications.

Li ion batteries and Cu sulfidation has been studied with soft x-ray spectroscopy.

7. Summary in Swedish

Under de senaste fyra åren har jag studerat den elektroniska strukturen hos material som är relevanta för energiomsättningen. Jag har främst använt mig av två spektroskopiska metoder: röntgenabsorptionsspektroskopi (XAS) och resonant inelastiskt röntgen spridning (RIXS), vilket initialt ger information om respektive de tomma och fyllda tillstånd hos atomorbitaler. Med dessa karakteriseringar kan man utforska vad som händer på atomär nivå och därmed kunna förbättra processen som undersöks.

Jag har designat en reaktionscell som gör det möjligt att undersöka den partiella oxidationen av eten över en silverkatalysator under förhållanden som är relevanta för den industriella processen, dvs. vid 1 atm och 230°C. Här har vi funnit att det är kortvariga syretillstånd som kan påverka processen. Till exempel har vi funnit starka belegg för att molekylärt syre binder till silverytan vid 230°C.

Vi fann också spektroskopiska syresignaler som bara gick att upptäcka när den partiella oxidationen inte pågick. Detta kan indikera att denna typ av syre konsumeras i processen och att den hastighet med vilken det är möjligt för denna typ av syre att främställas sätter en gräns för hastigheten hos reaktionen.

Vi har också gjort mätningar på Li-ion batterier och har funnit att den initiala kristallstrukturen hos anodmaterialet $\text{Ni}_{0.5}\text{TiOPO}_4/\text{C}$ inte kan vara verksam på ett sätt som tidigare har antagits. Vi finner att nedbrytningen av kristallen skapar ett aktivt amorft område.

Katodmaterialet $\text{Li}_{2-x}\text{MnSiO}_4$ har också undersökts: här fann vi att en förändring av oxidationstillståndet hos Mn när den går från +3 till +4 gjorde att materialets kristallstruktur gick förlorat. Vidare fann vi att Mn inte är redox-aktivt som tidigare antagits i den första delen av uppladdningen, däremot fanns det förändringar hos kisel-syre nätverket.

Mätningar som vi har gjort på sulfideringen av oxiderat Cu har vidare bekräftat att disproportioneringsreaktionen, $\text{Cu}^{2+} + \text{Cu} \rightarrow 2\text{Cu}^+$, är avgörande för att sulfideringen kan ske. Detta innebär att om man till exempel vill använda Cu i den slutliga förvaringen av kärnbränsle i en miljö där sulfid är löst i vatten, så ger det extra säkerhet om det kan växa ett tjockt lager av oxider på Cu.

References

- [1] Joachim Stöhr. *NEXAFS spectroscopy*, volume 25. Springer, 1992.
- [2] Frank De Groot. High-resolution x-ray emission and x-ray absorption spectroscopy. *Chemical Reviews*, 101(6):1779–1808, 2001.
- [3] Jan-Erik Rubensson. Rixs dynamics for beginners. *Journal of Electron Spectroscopy and Related Phenomena*, 110 - 111(0):135 – 151, 2000. Soft X Ray Emission Spectroscopy.
- [4] Johan Forsberg. *In Situ Soft X-ray Spectroscopies Applied to Atmospheric Corrosion And Related Systems*. PhD thesis, Uppsala University, Department of Physics and Materials Science, 2009.
- [5] Opto Diode Corporation. Axuv100eut##, 2013.
- [6] J Nordgren, G Bray, S Cramm, R Nyholm, J-E Rubensson, and N Wassdahl. Soft x-ray emission spectroscopy using monochromatized synchrotron radiation. *Review of Scientific Instruments*, 60:1690, 1989.
- [7] Hendrik A Kramers and Werner Heisenberg. Über die streuung von strahlung durch atome. *Zeitschrift für Physik A Hadrons and Nuclei*, 31(1):681–708, 1925.
- [8] B.L. Henke, E.M. Gullikson, and J.C. Davis. X-ray interactions: Photoabsorption, scattering, transmission, and reflection at $e = 50\text{-}30,000$ ev, $z = 1\text{-}92$. *Atomic Data and Nuclear Data Tables*, 54(2):181 – 342, 1993.
- [9] Y.-P. Sun, Q. Miao, A. Pietzsch, F. Hennies, T. Schmitt, V. N. Strocov, J. Andersson, B. Kennedy, J. Schlappa, A. Föhlich, F. Gel'mukhanov, and J.-E. Rubensson. Interference between resonant and nonresonant inelastic x-ray scattering. *Phys. Rev. Lett.*, 110:223001, May 2013.
- [10] Recognizing the best in innovation: Breakthrough catalyst. *R&D Magazine*, (879):20, 2005.
- [11] Carlo Lamberti, Adriano Zecchina, Elena Groppo, and Silvia Bordiga. Probing the surfaces of heterogeneous catalysts by in situ ir spectroscopy. *Chem. Soc. Rev.*, 39:4951–5001, 2010.
- [12] B. Hammer, Y. Morikawa, and J. K. Nørskov. Co chemisorption at metal surfaces and overlayers. *Phys. Rev. Lett.*, 76:2141–2144, Mar 1996.
- [13] F LYON. 1,3-butadiene, ethylene oxide and vinyl halides (vinyl fluoride, vinyl chloride and vinyl bromide). *IARC Monographs on the Evaluation of Carcinogenic Risks to Humans*, 97:185 – 287, 2008.
- [14] SRI Consulting. Wp report - ethylene oxide, Jan 2009.
- [15] Valerii I. Bukhtiyarov and Axel Knop-Gericke. Chapter 9 ethylene epoxidation over silver catalysts. In *Nanostructured Catalysts: Selective Oxidations*, pages 214–247. The Royal Society of Chemistry, 2011.
- [16] V. I. Bukhtiyarov, M. Hävecker, V. V. Kaichev, A. Knop-Gericke, R. W. Mayer, and R. Schlögl. Atomic oxygen species on silver: Photoelectron spectroscopy and x-ray absorption studies. *Phys. Rev. B*, 67:235422, Jun 2003.

- [17] Suljo Linic, Jerome Jankowiak, and Mark A. Barteau. Selectivity driven design of bimetallic ethylene epoxidation catalysts from first principles. *Journal of Catalysis*, 224(2):489 – 493, 2004.
- [18] Axel Knop-Gericke, Evgueni Kleimenov, Michael Hävecker, Raoul Blume, Detre Teschner, Spiros Zafeiratos, Robert Schlögl, Valerii I. Bukhtiyarov, Vasily V. Kaichev, Igor P. Prosvirin, Alexander I. Nizovskii, Hendrik Bluhm, Alexei Barinov, Pavel Dudin, and Maya Kiskinova. Chapter 4 x-ray photoelectron spectroscopy for investigation of heterogeneous catalytic processes. volume 52 of *Advances in Catalysis*, pages 213 – 272. Academic Press, 2009.
- [19] Volkmar Zielasek, Birte Jürgens, Christian Schulz, Jürgen Biener, Monika M Biener, Alex V Hamza, and Marcus Bäumer. Gold catalysts: nanoporous gold foams. *Angewandte Chemie International Edition*, 45(48):8241–8244, 2006.
- [20] X Bao, M Muhler, B Pettinger, Y Uchida, G Lehmppfuhl, R Schlögl, and G Ertl. The effect of water on the formation of strongly bound oxygen on silver surfaces. *Catalysis letters*, 32(1-2):171–183, 1995.
- [21] EM Sadvovskaya, DA Bulushev, and BS Bal'zhinimaev. Dynamics of isotopic label transfer in catalytic reactions. *Kinetics and catalysis*, 40(1):54–61, 1999.
- [22] B. S. Balzhinimaev. *Kinetics and Catal.*, 40(879), 1999.
- [23] J.G Serafin, A.C Liu, and S.R Seyedmonir. Surface science and the silver-catalyzed epoxidation of ethylene: an industrial perspective. *Journal of Molecular Catalysis A: Chemical*, 131(1-3):157 – 168, 1998.
- [24] Peter Glans, K Gunnelin, P Skytt, JH Guo, Nial Wassdahl, J Nordgren, H Ågren, F Kh Gel'Mukhanov, T Warwick, Eli Rotenberg, et al. Resonant x-ray emission spectroscopy of molecular oxygen. *Physical review letters*, 76(14):2448–2451, 1996.
- [25] H. M. Tong, G. Arjavalingam, R. D. Haynes, G. N. Hyer, and J. J. Ritsko. High-temperature thin-film pt–ir thermocouple with fast time response. *Review of Scientific Instruments*, 58(5):875–877, 1987.
- [26] Simone Piccinin, Spiros Zafeiratos, Catherine Stampfl, Thomas W Hansen, Michael Hävecker, Detre Teschner, Valerii I Bukhtiyarov, Frank Girgsdies, Axel Knop-Gericke, Robert Schlögl, et al. Alloy catalyst in a reactive environment: The example of ag-cu particles for ethylene epoxidation. *Physical review letters*, 104(3):035503, 2010.
- [27] Suljo Linic, Jerome Jankowiak, and Mark A Barteau. Selectivity driven design of bimetallic ethylene epoxidation catalysts from first principles. *Journal of Catalysis*, 224(2):489–493, 2004.
- [28] Malin B Johansson, Gustavo Baldissera, Iryna Valyukh, Clas Persson, Hans Arwin, Gunnar A Niklasson, and Lars Österlund. Electronic and optical properties of nanocrystalline wo 3 thin films studied by optical spectroscopy and density functional calculations. *Journal of Physics: Condensed Matter*, 25(20):205502, 2013.
- [29] Malin B. Johansson, Gunnar A. Niklasson, and Lars Österlund. Structural and optical properties of visible active photocatalytic wo3 thin films prepared by reactive dc magnetron sputtering. *Journal of Materials Research*, null:3130–3140, 12 2012.
- [30] Haidong Zheng, Jian Zhen Ou, Michael S Strano, Richard B Kaner, Arnan

- Mitchell, and Kourosch Kalantar-zadeh. Nanostructured tungsten oxide—properties, synthesis, and applications. *Advanced Functional Materials*, 21(12):2175–2196, 2011.
- [31] T. van der Meulen, A. Mattson, and L. Osterlund. A comparative study of the photocatalytic oxidation of propane on anatase, rutile, and mixed-phase anatase-rutile tio₂ nanoparticles: Role of surface intermediates. *Journal of Catalysis*, 251(1):131 – 144, 2007.
- [32] Gaskatel. Ag/agcl reference electrode siref, August 2013.
- [33] Hao-Jie Song, Zhao-Zhu Zhang, and Xue-Hu Men. Superhydrophobic peek/ptfe composite coating. *Applied Physics A*, 91(1):73–76, 2008.
- [34] O. Fuchs. *Soft X-ray Spectroscopy of Organic Molecules and Liquids*. 2009.
- [35] J-M Tarascon and Michel Armand. Issues and challenges facing rechargeable lithium batteries. *Nature*, 414(6861):359–367, 2001.
- [36] Håkan Hollmark. *Redox Reactions in Li-ion Battery Cycling and in Cu Corrosion Studied by Soft X-ray Spectroscopy*. PhD thesis, Uppsala University, Department of Physics and Astronomy, 2011.